

A Global Evaluation of Daily to Seasonal Aerosol and Water Vapor Relationships Using a Combination of AERONET and NAAPS Reanalysis Data

Juli I. Rubin¹, Jeffrey S. Reid², Peng Xian², Christopher M. Selman¹, and Thomas F. Eck^{3,4}

¹U.S. Naval Research Laboratory, Washington, DC, 20375, USA

²U.S. Naval Research Laboratory, Monterey, CA, 93943, USA

³NASA Goddard Space Flight Center, Greenbelt, MD, 20771, USA

⁴Goddard Earth Sciences Technology and Research (GESTAR) II, University of Maryland Baltimore County, Baltimore, MD 21250, USA

Correspondence to: Juli I. Rubin (juli.rubin@nrl.navy.mil)

Abstract. The co-transport of aerosol particles and water vapor has long been noted in the literature, with a myriad of implications ~~from such as~~ air mass characterization, ~~to~~ radiative transfer, ~~and data assimilation~~. ~~Here, in this study,~~ the relationship between aerosol optical depth (AOD) and precipitable water vapor (PW) is evaluated to our knowledge for the first time globally, at daily to seasonal levels using approximately 20 years of AERONET observational data and the 16-year NAAPS reanalysis v1.0 (NAAPS-RA) model fields. The combination of AERONET observations with small ~~associated~~ uncertainties and the reanalysis fields with ~~full~~ global coverage is used to provide a best estimate of the seasonal AOD and PW relationships, including an evaluation of correlations, slope, and PW probability distributions for identification of statistically significant differences in PW for high AOD events. The relationships produced from the AERONET and NAAPS-RA datasets were compared against each other and showed consistency, indicating that the NAAPS-RA provides a realistic representation of the AOD and PW relationship. The ~~initial~~ analysis ~~is then extended to include~~ layer AOD and PW relationships for proxies of the planetary boundary layer, and lower, middle and upper free troposphere. ~~It was found that t~~he dominant AOD and PW relationship is positive, supported by both AERONET and model evaluation, which varies in strength by season and location. These relationships were found to be statistically significant and present across the globe, observed on an event by event level. Evaluations at individual AERONET sites implicate synoptic-scale transport as a contributing factor in these relationships at daily levels. Negative AOD and PW relationships were identified and predominantly associated with regional dry season timescales in which biomass burning is the predominant aerosol type. This is not an indication of dry air association with smoke ~~aerosol~~ for an individual event, but is ~~more~~ a reflection of the overall dry conditions leading to more biomass burning and higher associated AOD values. Stronger correlations between AOD and PW are found when evaluating the data by vertical layers, including boundary layer, lower/middle/upper free troposphere (corresponding to typical water vapor channels), with the largest correlations observed in the free troposphere—indicative of aerosol and water vapor transport events. By evaluating variability between PW and relative humidity in the NAAPS-RA, hygroscopic growth was found to ~~be a dominant term to~~ 1) amplify positive AOD-PW relationships, particularly in the mid-latitudes; 2) diminish negative relationships in dominant biomass burning regions; and 3) ~~leads to~~ statistically insignificant changes in PW for high AOD events ~~in ocean for maritime~~ regions. The importance of hygroscopic growth in these relationships indicates that PW is a useful tracer for AOD, ~~or light extinction~~, but not necessarily as strongly for aerosol mass. Synoptic-scale African dust events are an exception where PW is a strong tracer for aerosol ~~transport~~ shown by strong relationships even with hygroscopic ~~affects~~ effects. Given ~~these~~ results, PW can be exploited in coupled aerosol and meteorology data assimilation for AOD and the collocation of aerosol and water vapor should be carefully taken into account when ~~conducting particulate matter (PM) retrievals from space and in~~ evaluating radiative impacts of aerosol, with the season and location in mind.

44 **DISTRIBUTION STATEMENT A. Approved for public release. Distribution is unlimited.**

45 **1.0- Introduction**

46 The definition of an aerosol is that it is a colloidal system of particles or droplets suspended in a dispersed gaseous
47 medium (American Meteorological Society, 2020). While the word “aerosol” is often taken to represent only the
48 particulate phase, the true definition reminds us of the thermodynamic, compositional and radiative “whole” that
49 makes up the particulate and dispersed phases of an aerosol parcel. With this definition in mind, an important aspect
50 of aerosol parcels that should be considered is the covariability between the aerosol particles and the dispersed water
51 vapor. While the aerosol and water vapor relationship is generally accounted for in the context of relative humidity,
52 hygroscopicity, and optical properties (e.g., Hänel et al., 1976; Charlson et al. 1992), the covariability of aerosol
53 particles and dispersed water vapor is important in its own right. Early studies of co-located aerosol and water vapor
54 measurements demonstrated the structural covariability between the two components (e.g. Stull and Eloranta 1984;
55 Kleinman and Daum, 1991; Turner 2002; De Tomasi and Perrone, 2003). Now, coupled aerosol-water vapor profiles
56 are commonly used to infer aerosol layer structure (e.g., Livingston et al., 2003; Reid et al., 2003; 2008; 2019; Wang
57 et al. 2012; Yufeng et al., 2018), cloud detrainment (Su et al., 2011; Reid et al., 2019; He et al., 2021) and mixed layer
58 properties (Späth et al., 2016). Even integrated aerosol optical depth (AOD) and precipitable water vapor (PW)
59 comparisons have utility and have been used to identify air masses, transport pathways, and aerosol optical properties.
60 Regional studies include Africa (Kumar et al., 2017, Xian et al. 2020), the Amazon (Kaufman and Frasier, 1997;
61 Martins et al., 2018), India (Kumar et al., 2013; and Kannemadugu et al., 2015), and North America (O’Neil et al.,
62 1993; Smirnov et al., 1994). Notable examples of co-transport of aerosol particles and water vapor include the African
63 Monsoon Multidisciplinary Analysis (AMMA) in which elevated biomass burning aerosol layers were found with
64 higher water vapor concentrations than the surrounding air (Kim et al. 2009). Likewise, Marsham et al., 2016
65 investigated water vapor enhancements with dust in the Saharan Air Layer (SAL).

66
67 ~~High should be noted that~~ higher PW amounts are typically associated with higher cloud cover fractions. These higher
68 cloud fractions create additional environmental conditions for enhancements of the aerosol AOD and PW relationship.
69 There is a high RH halo around cumulus clouds (Radke and Hobbs, 1991; Perry and Hobbs, 1996) which increases
70 the near cloud hygroscopic growth of aerosol. Additionally, the passage of aerosol through clouds by convection
71 and/or advection also increases hygroscopic growth. Cloud processing of particles in cloud droplets and new particle
72 formation from gas-to-particle reactions in cloud water droplets are also important. Examples of remote sensing
73 observations from AERONET of cloud processing increasing AOD in layer clouds and/or fog are given in Eck et al.
74 (2012) and in the vicinity of cumulus clouds in Eck et al. (2014). Additionally high AOD events were often found to
75 be associated with clouds in East Asia (Eck et al., 2019; Arola et al., 2017).

76
77 In addition to its utility as a tracer for transport and mixing, the aerosol particle-water vapor co-transport are significant
78 in regards to their relative contributions to overall solar and terrestrial radiative effects (Rosario et al., 2011; Marsham
79 et al., 2016; Deaconu et al., 2019; Gutleben et al., 2019; Granados-Muñoz et al., 2019; Zhu et al., 2019; Yu et al.,
80 2021). Similarly, co-transport must be considered in atmospheric correction of land, ocean and atmospheric products

81 (e.g., Sobrino et al. 1993; Eck and Holben 1994; DeSouza-Machado et al., 2006; Luo et al., 2019; Zeng et al., 2017;
82 Patadia et al., 2018; Frouin et al. 2019, Ibrahim et al. 2019; Miller et al. 2019). As previously noted, there are also
83 links to cloud development and potentially indirect effects (Ten Hoeve et al., 2011; Pistone et al., 2016). Ultimately,
84 the coupled aerosol particle- water vapor system must be considered jointly to adequately contain overall climate
85 budgets and forcing (Kaufman and Fraser, 1997; Wong et al., 2009; Schneider et al, 2010; Sherwood et al, 2010;
86 Haywood et al., 2011; Huttunen et al., 2014; Yu et al., 2014; Spyrou 2018).

87
88 Finally, recent advances in coupled data assimilation (DA) allow for not only a joint analysis of aerosol particles and
89 water vapor as is done in weakly coupled approaches, but for observations to jointly influence posteriors through
90 cross-covariances in strongly coupled DA (Liu et al., 2011; Lee et al., 2017; Ménard et al., 2019). The hope is that
91 strongly coupled DA can be used to generate a more consistent representation of coupled atmospheric systems. In the
92 context of the aforementioned references on the coupled aerosol particle-water vapor system, there is now a more
93 pressing need for evaluating joint aerosol and water vapor measurements. This is further emphasized by the observed
94 frequency of aerosol and water vapor co-transport in both forecast models and satellite observations. Similar spatial
95 patterns between aerosol optical depth (AOD) and precipitable water vapor (PW) can be observed on a daily basis in
96 model analyses, forecasts, and satellite products such as the Morphed Integrated Microwave Imagery at CIMSS - Total
97 Precipitable Water (MIMIC-TPW) (Wimmers et al. 2011), particularly associated with mid-latitude fronts. An
98 example of forecasts of TPW and AOD from the Navy Global Environmental Model (NAVGEM) (Hogan et al. 2014)
99 and Navy Aerosol Analysis Prediction System (NAAPS; Lynch et al. 2016), respectively are shown in Figure 1 in
100 which co-transport regions are highlighted. Aerosol and water vapor relationships are not expected to be universal and
101 will likely vary in magnitude from air mass to air mass due to differences in sources, physics, and overall vertical
102 distribution. While the previously mentioned studies have found relationships between aerosol and water vapor for a
103 host of case or local studies, this relationship has not to our knowledge been evaluated on a larger spatial and temporal
104 scale for broad applicability for aerosol forecasting and data assimilation.

105
106 This is the first of several studies developing coupled data analysis and assimilation of the water vapor- aerosol particle
107 system. Here, the project begins by focusing on observations of synoptic scale temporal and spatial relationships using
108 the extensive NASA Aerosol Robotic Network (AERONET; Holben et al., 1998; Giles et al., 2019). The advantage
109 of AERONET for this study is that the data record is long and includes high frequency ground-based measurements
110 of both aerosol in the form of AOD and water vapor in the form of PW with sites located across the globe. Additionally,
111 AERONET measurements are made throughout the entire daylight hours when the sun is not obscured by clouds. It
112 should be noted that this does result in a high pressure bias in AERONET data since few measurements are possible
113 in extensive cloud fraction conditions. Another important advantage is that the observations can be made effectively
114 in the near vicinity of clouds without the commonly observed satellite measurement artifacts of multiple scattering
115 between clouds, molecules, and particles which enables a minimization of cloud contamination in the near vicinity of
116 clouds as compared to satellite observations. While the AERONET network is extensive, it cannot provide a full global
117 evaluation of the aerosol and water vapor relationship. Therefore, the relationships identified in the AERONET dataset
118 are compared against model AOD and PW relationships found in the NAAPS reanalysis (NAAPS-RA) dataset (Lynch

119 et al. 2016). A description of both the AERONET and NAAPS-RA datasets and the analyses conducting for
120 quantifying the global AOD and PW relationships are described in the Methods section below. The results of the
121 analysis are discussed in the context of large-scale relationships between column-integrated AOD and PW. A follow-
122 on study will then take the relationships found in this work and move on to evaluate the relationships on an event level
123 in space and time as well as the controlling factors that drive the aerosol and water vapor relationship, in particular,
124 how much synoptic scale transport controls the observed covariability.

125

126 **2 Methods**

127 In order to evaluate the relationship between column-integrated aerosol and water vapor in space and time, the
128 AERONET observational network is used as it provides joint measurements of aerosol and water vapor with low
129 levels of uncertainty, has a large number of sites located across the globe, and a long data record. While AERONET
130 measurements are column-integrated, they provide a good starting point for understanding the observed aerosol and
131 water vapor relationships at locations across the globe. As a first step, relationships are quantified at AERONET sites
132 between daily-averaged AOD and PW measurements. The focus here is on the synoptic-scale relationships between
133 aerosol and water vapor. Therefore, daily-averaged relationships are evaluated in this analysis, using correlations and
134 an evaluation of the water vapor probability distributions to identify statistically significant changes in PW with AOD.
135 The evaluation is then extended to the NAAPS-RA dataset in order to provide a more complete global perspective in
136 the full column as well as in different vertical components of the atmosphere, including the boundary layer and free
137 troposphere, as a means to understand how these relationships vary when considering vertical position. Finally, the
138 impact of relative humidity and hygroscopic growth covariability on model predicted AOD and PW relationships is
139 evaluated.

140 **2.1 Data Description:**

141 **2.1.1 AERONET AOD**

142 AERONET is a global ground-based network of sun photometers that measure direct sun and sky radiances over a
143 range of wavelengths (340-1640nm). These measurements are used to generate column-integrated aerosol properties
144 of AOD and aerosol microphysical and radiative properties (Holben et al. 1998; Giles et al., 2019). The network
145 includes over 600 sites with data available at <https://aeronet.gsfc.nasa.gov/>. The uncertainty in AERONET AOD is
146 reported to be ~0.01–0.02 for level 2 data with the higher uncertainty of 0.02 pertaining to the UV wavelengths and
147 the lower ~0.01 uncertainty associated with visible and near infrared wavelengths (Eck et al., 1999). Due to this low
148 uncertainty, AERONET AOD observations are used for validation of satellite retrievals (Remer et al. 2002, Ichoku
149 et al. 2002, Kahn et al. 2005) as well as for verification of model forecasts (Zhang et al. 2008, Benedetti et al. 2008,
150 Sessions et al. 2015, Xian et al. 2019). For this analysis, AERONET version 3 (Giles et al. 2019), level 2 daily-
151 averaged AOD observations are used. AERONET AOD observations at 675nm for all available sites were collected
152 and sites that had a minimum of 100 daily-averaged values were retained for the analysis, with seasonal data counts
153 in Figure 2. The 675nm wavelength was selected as it is a core AERONET wavelength that is available at all sites
154 and provides parity for both the fine and coarse aerosol modes. It should be noted that the AERONET-Maritime
155 Aerosol Network (MAN) data is not included in this analysis as MAN data is shipborne and available on a periodic
156 basis, and thus is not consistent with the long-term evaluation at fixed points that is conducted in this work.

157

158

159 2.1.2 AERONET Water Vapor

160 Precipitable water vapor (PW), a measure of the total amount of water vapor contained in a vertical column from the
161 surface to the top of the atmosphere, is retrieved from AERONET direct sun irradiance measurements in the water
162 vapor absorption band around 940nm. The uncertainty of AERONET water vapor data is reported at 12% (Sano et al.
163 2003) and more recently, an analysis of uncertainty against radiosonde, microwave radiometry, and GPS data indicated
164 a dry bias of 5-6 % and a total estimated uncertainty of 12-15% (Perez-Ramirez et al. (2014)). The Perez-Ramirez et
165 al. (2014) evaluation with the identified uncertainty range of 12-15% included PW retrieval comparison at 3 sites
166 located in the tropics, mid-latitudes and the arctic, covering a range of climatic conditions and temperature/water vapor
167 profiles, and therefore, provides a reasonable uncertainty estimate for the entire AERONET network. The PW data
168 used in this analysis comes from the same AERONET version 3, level 2 daily-averaged dataset that is used for the
169 AOD data. As was the case for the AERONET AOD data, sites that had a minimum of 100 daily-averaged values
170 were retained for the analysis (Figure 2).

171

172 2.1.3 NAAPS Reanalysis

173 The NAAPS aerosol reanalysis v1.0 (Lynch et al. 2016) is a standardized global modal AOD product generated by
174 the U.S. Naval Research Laboratory (NRL) that extends over a 16 year time period (2003-2019). The core of the
175 aerosol reanalysis is the NAAPS offline aerosol transport model and its associated 2-dimensional variational data
176 assimilation system, the Navy Variational Data Assimilation System for Aerosol Optical Depth (NAVDAS-AOD).
177 NAAPS has been run semi-operationally at NRL since 1998 and became operational at the Fleet Numerical
178 Meteorology and Oceanography Center (FNMOC) in 2006 with NAVDAS-AOD operationally implemented in 2010.
179 For the NAAPS-RA, NAVDAS-AOD is used to assimilate quality-assured and quality-controlled AOD retrievals
180 from the Moderate Resolution Imaging Spectroradiometer (MODIS) and Multi-angle Imaging SpectroRadiometer
181 (MISR). AERONET AOD is not assimilated in the NAAPS-RA.

182

183 NAAPS generates 3-dimensional forecasts of dust, smoke, sea salt and a combined anthropogenic/biogenic fine
184 aerosol (ABF, also referred to in this work as pollution) mass concentration fields and the associated 3-dimensional
185 aerosol extinction and column-integrated AOD fields. As an offline model, NAAPS is driven by meteorological fields
186 from the Navy Global Environmental Model (NAVGEM) (Hogan et al. 2014), using analysis fields every 6 hours and
187 forecasts provided at 3 hour intervals. The NAVGEM analysis fields are generated using NAVDAS for assimilation
188 of a large number of conventional and satellite-based observations (Daley and Barker, 2001). NAVGEM variables
189 used by NAAPS includes the topography, sea ice, snow cover, surface stress, surface heat/moisture fluxes,
190 precipitation, lifting condensation level, cloud cover and height as well as 3-dimensional winds, temperature, and the
191 most relevant for this work, humidity. For the NAAPS analysis, aerosol sources, including dust and smoke, and
192 deposition processes were regionally tuned to best match observations (AERONET, MODIS). A detailed description
193 of the NAAPS-RA v1.0 is described in Lynch et al. 2016.

194

195 In NAAPS, the Hanel (1976) formulation of the hygroscopic growth factor (f) for a given species i and relative
196 humidity (r) is used to represent the effect of humidity on particle light scattering, defined as:

$$197 f_i(r) = \left[\frac{(1-r)}{(1-r_0)} \right]^{-\gamma_i}, \quad (1)$$

198 where γ_i is an empirical species-dependent exponent (anthropogenic/biogenic fine (ABF) =0.5 assuming 40% sulfate
199 and 60% organics, smoke=0.18, sea salt = 0.46, dust=0) and r_0 is the reference relative humidity of 30%. The
200 hygroscopic growth factor is applied when calculating the aerosol scattering coefficient. In order to assess the impact
201 of hygroscopic growth on model-predicted AOD and PW correlations, a “dry” AOD is also calculated for the NAAPS-
202 RA in which the hygroscopic growth factor is not applied.

203 For this work, the NAAPS-RA v1.0 AOD fields and the NAVGEM humidity fields used in generating the NAAPS-
204 RA are extracted for the full 16 year dataset (2003-2019). NAVGEM humidity fields were integrated vertically to
205 generate model-predicted PW fields and both the PW and AOD fields were averaged on a daily basis. Additionally,
206 “dry” AOD fields were calculated for the NAAPS-RA and likewise, averaged on a daily basis.

207 2.2 AOD and PW Relationship Analysis:

208 2.2.1 Correlation Analysis

209 As a first step in understanding the relationship between aerosol and water vapor in the AERONET data record,
210 correlations (Pearson correlation coefficients) are calculated at each AERONET site with a minimum of 100 data
211 points. The correlations are calculated between the daily-averaged AOD (675nm) and PW datasets seasonally
212 (December-January-February (DJF), March-April-May (MAM), June-July-August (JJA), September-October-
213 November (SON)). This analysis is used to identify when and where relationships exist between AOD and PW in the
214 data record and the strength of the relationship. In order to provide global context to the AERONET AOD and PW
215 correlations, the same analysis was conducted using the NAAPS 16-year v1.0 reanalysis dataset. The seasonal
216 reanalysis correlations were calculated in a similar manner as the AERONET data, using daily-averaged model-
217 generated AOD and PW values. The model-generated values were then compared against observationally generated
218 AERONET correlations. The correlations in both the AERONET and NAAPS-RA evaluation were tested for
219 statistical significance at the 95% confidence level.

220 2.2.2. Slope Evaluation

221 In addition to the AOD and PW Pearson correlation coefficients calculated from the AERONET and NAAPS-RA
222 datasets, the slopes of the AOD and PW relationship were calculated from the seasonal data using a Theil-Sen
223 regression. A Theil-Sen regression is a robust method for fitting a line to sample points by choosing the median of
224 slopes of all lines through pairs of points. Due to the use of the median slope, the Theil-Sen method is insensitive to
225 outliers and therefore, a useful method for this analysis. With the Theil-Sen regression, a 95 % confidence interval of
226 the Theil-Sen slope was calculated for each location and season.

227 2.2.3 Evaluation of the AOD and PW Probability Distribution

228 In addition to a correlation and slope analysis, the AOD and PW probability distributions were also evaluated. Given
229 the expectation that aerosol and water vapor relationships will change depending on the air mass, seasonal correlations
230 can obscure the presence of aerosol and water vapor relationships when air masses with an existing relationship
231 between aerosol and water vapor occur infrequently. In this evaluation, the PW distribution associated with high AOD
232 events, defined as having an AOD value greater than 1 standard deviation above the mean, were compared to the PW
233 distribution for all data for a given location and season. A t-test was conducted to identify statistically significant
234 differences in the PW distribution means for the high AOD events and all data (p-value = 0.05). This analysis was
235 conducted seasonally (DJF, MAM, JJA, SON) using both the AERONET and the NAAPS-RA datasets.

236 **2.2.4 Vertical Evaluation of the AOD and PW Relationship**

237 While the global and AERONET site AOD and PW evaluations as well as the studies cited in the introduction provide
238 an understanding of the column-integrated relationship between aerosol and water vapor, an additional evaluation was
239 conducted to look at the aerosol and water vapor relationship in different levels of the troposphere. This evaluation
240 was conducted using the NAAPS-RA fields only, since observations of joint aerosol and water vapor vertical structure
241 are limited. Model generated correlations were calculated for a defined boundary layer (BL), lower free troposphere
242 (LT), mid-free troposphere (MT), and upper free troposphere (UT) region. The reanalysis total aerosol extinction and
243 specific humidity were vertically integrated in the first 1km of the atmosphere as a representation of the boundary
244 layer. Integration levels in the free troposphere were selected based on the sensitivities of the upper, mid-level, and
245 lower-level geostationary water vapor channels on the NOAA Geostationary Operational Environmental Satellite
246 (GOES) Advanced Baseline Imager (ABI) and the JMA Advanced Himawari Imager (AHI) with a goal of using these
247 water vapor channels to further explore aerosol and water vapor relationships in future work. The selected integration
248 levels were from 800 to 500 hPa (LT), 600 to 300 hPa (MT), and 400 to 300 hPa (UT), respectively. The vertically
249 integrated relationships, as was done for the full column-integrated evaluation, are calculated seasonally and are used
250 to identify if the model correlations are controlled by aerosol and water vapor in certain parts of the atmosphere. While
251 the boundary layer is expected to be a dominant control of the signal, given the sources of both aerosol and water
252 vapor are within the boundary layer, strong correlations within the free troposphere could indicate aerosol and water
253 vapor relationships as a result of lifting from the surface or long-range transport which typically occurs within the free
254 troposphere.

255 **2.2.5 Impact of Hygroscopic Growth on AOD and PW relationships**

256 It is well documented in the literature that water uptake on aerosol particles under moist conditions impacts aerosol
257 optical properties. Because of this, it is necessary to understand how much hygroscopic growth impacts AOD and PW
258 relationships through covariability of PW and relative humidity. The data to evaluate this observationally is not
259 available, therefore, the NAAPS-RA is used to evaluate the impact of the hygroscopic growth factor on model
260 predicted correlations. As a first step in this evaluation, the correlation between PW and relative humidity was
261 calculated by season for the previously defined vertical components of the atmosphere (boundary layer,
262 lower/mid/upper free troposphere). In order to calculate relative humidity for each defined part of the troposphere, a
263 saturation specific humidity was calculated in each model level using the reanalysis pressure and temperature fields

264 as input. Both the specific humidity and the saturation specific humidity were vertically integrated over the defined
265 levels and the ratio of the two values was used to produce a relative humidity that conserves the amount of water vapor
266 through the associated portion of the troposphere. This analysis gives a first look at where the covariability between
267 PW and RH is expected to be most impactful on the AOD and PW relationship. However, given aerosol hygroscopic
268 growth is dependent on aerosol type, the analysis was taken a step further by calculating the seasonal relationships,
269 including correlations/slopes and the probability distribution evaluation, between dry AOD and PW. The dry AOD,
270 in which the impact of hygroscopic growth on AOD is removed as described in the NAAPS-RA section (2.1.3), was
271 calculated for the full dataset. The relationships using the dry AOD are compared to the standard AOD/PW results as
272 a means to evaluate the impact of hygroscopic growth on the modeled AOD and PW relationships.

273 **2.2.6 Evaluation at Individual AERONET Sites**

274 While the previous analyses provide a global perspective on the aerosol and water vapor relationships, the relationships
275 were also evaluated at select AERONET sites to provide a first look at what is driving the observed covariability
276 between AOD and PW on an event level. The AERONET sites, including Tallahassee, Florida in the Southeast United
277 States, Beijing, China in East Asia, Izana, Canary Islands off the coast of Africa, and Alta Floresta, Brazil in South
278 America, are selected based on the strength of the observed/modeled relationships and cases are selected for different
279 seasons that exhibited both positive and negative relationships. While this evaluation does not by any means provide
280 a complete understanding of the drivers of these relationships across the globe, it can be used to provide some insight.

281 **3.0 Results**

282 This study is highly multi-dimensional. In order to elucidate the findings, the results are first presented as a global
283 evaluation, which is followed by a more in-depth discussion by region, level, and accounting for the impacts of
284 hygroscopicity. As aerosol regimes are typically seasonal in nature, all evaluations are performed for DJF-MAM-JJA-
285 SON. Summaries of the data used in the analyses are presented in Figures 2 through 6, including: Figure 2, seasonal
286 counts of daily-averaged AERONET AOD and PW data; Figure 3, seasonal mean AERONET and NAAPS-RA AOD
287 and PW values; Figure 4 seasonal NAAPS-RA AOD averages by aerosol types (dust, sea salt, anthropogenic/biogenic
288 fine, biomass burning); and Figures 5 and 6, the NAAPS-RA AOD and PW (respectively) 25th, 75th, and 90th
289 percentiles from daily data and associated interquartile range (IQR) of by season. In regards to the AERONET
290 analysis, only sites with a minimum of 100 data points are included, as previously discussed. Due to this constraint,
291 some temporary sites used for field campaigns are excluded in this work.

292 **3.1 Global Patterns of AOD-PW Correlation**

293 Overall, the seasonal patterns in both AOD and PW are pretty consistent between AERONET and the NAAPS-RA
294 (Figure 3). For example, peak AOD values in North America and Europe occur during the summer months in both
295 datasets. Likewise, peak AOD values are found over the Sahel in winter and spring due to a combination of dry-season
296 biomass burning and dust associated with the northeasterly Harmattan winds with shifts in peak AOD further north in
297 summer due to increased dust activity over the Sahara. Like the Sahel, peak AOD values associated with fire activity
298 during regional dry seasons are also found in both datasets for Central and South America, Southern Africa and

299 Southeast Asia. Boreal regions, which also exhibit seasonality due to fires in summer months, are not as well sampled
300 in the AERONET dataset, making it harder to see seasonal shifts in AOD. However, this seasonality is found in the
301 NAAPS-RA. Likewise, northward shifts in PW are seen in AERONET and the NAAPS-RA in the summer and a
302 southward shift in the winter months. A more in-depth discussion of the data by region, which is consistent with
303 verification regions presented in Lynch et al. (2016) and Rubin et al. (2016), is below:

- 304 1) North America: The largest number of AERONET sites are present in this region with ~180 included in the
305 analysis. AERONET data counts are the highest in the summer months (JJA) which also coincides with
306 peak mean AOD and PW values in both the AERONET and NAAPS-RA datasets (Figure 3). Summertime
307 peak AOD values are associated with ABF and smoke aerosol types, concentrated to the North, and a
308 combination of ABF and transported dust to the South (Figure 4). Despite JJA being associated with the
309 highest AOD values, the IQR is only around 0.1-0.2 (Figure 5). The 90th percentile AOD values in JJA for
310 North America are mainly associated with large smoke events, particularly originating from the Pacific
311 Northwest and Boreal regions (Figure 5). High AOD values are also observed in MAM months concentrated
312 in the Southeast United States (Figures 2 and 5), associated with smoke (originating from Central American
313 fires) and ABF/pollution aerosol types (Figure 5).
- 314 2) Europe: Data from ~125 AERONET sites was included in the analysis in Europe. Like the North America
315 region, peak AERONET data counts occur during JJA months (Figure 2). Peak AOD values are observed
316 during MAM and JJA (Figures 3 and 5), mainly associated with pollution in Eastern Europe, and
317 Mediterranean dust (Figure 4). PW values also peak during JJA (Figures 2 and 6). AOD IQR values, like
318 North America, are relatively small and on the order of 0.1-0.2 in JJA/MAM, with 90th percentile AOD
319 events in the 0.3-0.5 range.
- 320 3) East Asia: The analysis in East Asia included data from ~52 AERONET sites. AERONET data counts are
321 relatively consistent throughout the seasons (Figure 2). AOD values in East Asia are high throughout the year
322 due to the presence of pollution, concentrated to the East and dust, particularly in the spring and summer
323 (Figure 4). While pollution aerosol is present throughout the year, AOD values tend to be higher in the winter
324 months than the summer months in the NAAPS-RA (Figures 3 and 5) with the strength of the East Asian
325 Monsoon being a controlling factor in the spatial distribution and aerosol concentration in the region (Zhang
326 et al. 2010; Yan et al. 2011; Zhu et al. 2012; Mao and Liao, 2017). However, in the AERONET dataset, the
327 highest AOD values are observed in the summer months, consistent with the literature (Eck et al. 2005, 2018).
328 This discrepancy may be related to the satellite data that is assimilated in the NAAPS-RA in the summer
329 months. High AOD values are often misclassified as cloudy by the retrieval algorithms and subsequently
330 screened (Eck et al. 2018), which can contribute to low AOD biases in the model (Reid et al. 2022). The
331 range in AOD values is particularly large over East Asia as shown by the percentiles in Figure 5 with peak
332 IQR values of around 0.6-0.7 occurring during DJF.
- 333 4) South America: Data from ~44 AERONET sites was used in the analysis in South America. AERONET
334 data counts are the greatest during JJA and SON months, which is coincident with the highest AOD values.
335 This is particularly the case in SON, which is the dry season in South America when fire activity is increased.

336 The dominance of smoke aerosol is shown in the NAAPS-RA for these months (Figure 4). Extreme event
337 AOD values (90th percentile) and the IQR are the greatest for SON, again due to fire activity (Figure 5).

338 5) Northern Africa: Data from ~39 sites were used for evaluation in Northern Africa. Data counts are relatively
339 consistent across the seasons with the exception of the Banizoumbou, Niger site with approximately 1600
340 data points from 16 years of data during the DJF season. The AERONET and reanalysis average AOD values
341 for the North African Sahel region peaks in the winter and spring months (DJF, MAM) due to a combination
342 of dust and smoke aerosol (Figure 4). Peak Sahel AOD values coincide with the ITCZ being its most southern
343 position, which is shown in the PW fields (Figure 3 and 6). North Africa, particularly the Sahara, has high
344 AOD in the spring and summer months due to dust outbreaks with peak AOD values exceeding 1 and IQR
345 values in the 0.4-0.5 range (Figure 5).

346 6) Southern Africa: The analysis in Southern Africa included data from ~30 AERONET sites. AERONET data
347 counts are pretty consistent throughout the year, however, there are less sites available for analysis during
348 the DJF months. AOD values in Southern Africa are the highest in JJA and SON which is coincident with
349 peak fire activity in the region.

350 7) Arabian Peninsula: AERONET data counts from ~20 sites are consistent across the seasons in this region.
351 While dust emissions are present through the year, peak dust activity occurs in the summer months as shown
352 in the AERONET and NAAPS-RA AOD mean and percentile values (Figures 3 and 5).

353 8) India: The number of AERONET sites was ~20 in India with locations concentrated towards the North for
354 sampling the Indo Gangetic Plain in which pollution dominated AOD is present throughout the year, with
355 peak AOD values exceeding 1 during all seasons (Figure 3-5). Dust aerosol from the Thar Desert and the
356 Arabian Peninsula are transported to western India, particularly in the MAM and JJA seasons, while smoke
357 aerosol contributes to AOD in eastern India in MAM. AOD and PW are heavily influenced by the summer
358 monsoon season in which peak PW is observed (Figures 3 and 6).

359 9) Southeast Asia: Data from ~21 sites was available for the analysis in Southeast Asia. The number sites used
360 is greatest in the spring (Figure 2), coincident with the Peninsular Southeast Asia fire season in which peak
361 AOD values exceed 1 and large IQR values are present (Figure 5). Peak AOD values shift towards Insular
362 Southeast Asia during the SON months in which fire activity increases. Pollution is also present throughout
363 the year.

364 Regressions of AOD and PW for the daily data by season, including correlation coefficients and slopes, and the
365 statistically significant difference in mean PW between the distribution associated with high AOD events only and the
366 full PW distribution for both the NAAPS-RA and AERONET daily data are presented in Figure 7 with confidence
367 intervals on the Theil-Sen slopes shown in Figure 8. Red regions/sites indicate a positive correlation in which higher
368 PW is associated with higher AOD values and blue regions indicate a negative relationship in which lower PW is
369 associated with high AOD values. For all evaluations in Figure 7, the predominant signal is positive (ie. red) in both
370 the AERONET observations and the NAAPS-RA with the strongest correlations varying by season, and/or aerosol
371 regime. In the AERONET dataset, the strongest positive correlations are summarized in Tables 1-4 for DJF, MAM,
372 JJA, and SON, respectively. Also included are NAAPS-RA values for these sites as a means of comparison. For winter

373 months (DJF), the strongest positive correlations (>0.6) occur at sites in the Southeast United States, East Asia and
374 select sites in the Middle East such as Dhadnah, UAE (Table 1). In the spring months (MAM), dominant positive
375 relationships occur at mostly Eastern United States sites and the Nainital site in India (Table 2). Southern Africa sites
376 associated with smoke aerosol, Eastern European sites, and select sites in the Eastern United States have the strongest
377 positive correlations in the summer months (JJA) (Table 3, Figure 7). In the fall (SON), AERONET positive
378 correlations are strongest for the Eastern United States, select European sites as well as a site at Dhadnah, United Arab
379 Emirates.

380 The NAAPS-RA daily correlations (Figure 7) within seasonal aggregates indicate similar but not identical spatial
381 patterns relative to the AERONET dataset. The dominant positive correlation regions include the Eastern/Southeastern
382 United States as is found in AERONET. Likewise, stronger European AOD and PW correlations are found in the
383 summer months (JJA), in Eastern Asia in the winter season (DJF), and the Middle East in the fall (SON). The NAAPS-
384 RA results are helpful in that it provides a more complete perspective on the AOD and PW relationships. In addition
385 to strong positive correlations in Southeast United States and East Asia during DJF, the NAAPS-RA also indicates
386 strong positive correlations in parts of Southwest Asia (Iran/Afghanistan/Pakistan), India, South America, and
387 Southern Africa, which are minimally if not at all sampled by AERONET. The spatial extent of the observationally-
388 sampled relationships can also be seen. For example in MAM, the AERONET correlation at the Tamanrasset site in
389 Algeria is 0.55 with a consistent NAAPS-RA correlation of 0.53. In the reanalysis, the correlations, greater than 0.5,
390 extend to the east of Tamanrasset. Likewise, the spatial extent of correlations for maritime regions can be seen in the
391 reanalysis, where AERONET sites are rare. In JJA months, correlations at the Dahkla site in Morocco are 0.45 in the
392 AERONET dataset. Although the NAAPS-RA correlation at Dahkla is weaker ($R=0.31$), the positive relationship
393 observed in both datasets on the West coast of Africa can be seen extending out into the Atlantic ocean in the
394 reanalysis, consistent with dust transport pathways. Correlations associated with aerosol transport are also seen in
395 Southern Africa in the reanalysis, extending out into the ocean.

396 Although positive correlations are dominant throughout the world, negative correlations were also identified in both
397 the AERONET and NAAPS-RA datasets from daily data. In the AERONET dataset, negative correlations are limited
398 to the tropic/subtropics with negatively correlated regions mostly associated with biomass burning. The strongest
399 negative correlations in the AERONET dataset are shown in Tables 1-4 with NAAPS-RA values shown for
400 comparison. During all seasons, negative correlations are found in the Sahel region in both AERONET and the
401 NAAPS-RA with the negative relationships extending further northwards in the boreal spring and summer months.
402 This results in an exceptionally strong dipole between Saharan and Sahelian outflow and is likely related to shifts in
403 the ITCZ. This points to aerosol sources (biomass burning and dust) and scavenging as a cause of the negative AOD
404 and PW relationship. The NAAPS-RA shows these negative correlations extending into the Atlantic Ocean with
405 seasonally dependent differences. Negative correlations extend into the Caribbean in JJA and to northern parts of
406 South America in MAM, consistent with seasonal transport pathways. Other negative correlation regions include
407 Southeast Asia, South America, and Southern Africa. For these regions, the strongest negative correlations are
408 associated with the respective dry, burning seasons. For example, negative correlations are strongest in Peninsular

409 Southeast Asia in MAM and in Insular Southeast Asia and South America in SON. In these cases, negative AOD and
410 PW relationships are likely a result of higher aerosol emission occurring under dry conditions, which lead to more fire
411 activity. Southern Africa is an exception during JJA, in which smoke aerosol is dominant (Figure 4). However, this is
412 consistent with previous studies which have found elevated free tropospheric water vapor levels associated with
413 Southern African smoke events (Adebiyi et al. 2015; Pistone et al. 2021). Correlations in both AERONET and the
414 NAAPS-RA are positive in JJA and negative in MAM and SON when smoke aerosol is also present, but not at its
415 peak. One of the largest AERONET negative correlations occurs at the Jomsom, Nepal site in JJA with a value of -
416 0.65 (Table 3), although nearby sites show small or statistically insignificant correlations. The Jomsom site is located
417 at 2825 meters with maximum PW values around 2 while the nearby Pokhara site is 2000 meters lower in altitude
418 with maximum PW values around 5, therefore, Jomsom is likely a regional outlier due to altitude effects. For Jomsom
419 and the surrounding regions, the NAAPS-RA indicates no statistically significant correlation. While NAAPS and
420 AERONET are in general agreement in the locations of negative correlations, this discrepancy is likely related to meso
421 or small scale features, [including orography](#), that are not captured in a global, 1 degree model.

422

423 3.2 Consistency between AERONET and NAAPS-RA

424 While the global plots of AERONET and NAAPS-RA AOD and PW relationships give a sense of spatial agreement,
425 a scatterplot comparison of the quantitative values generated from the two datasets are used to take a closer look at
426 the consistency between the observed and predicted relationships. A seasonal comparison of AERONET and NAAPS-
427 RA regressions is shown as a scatterplot in Figure 9, including site by site a) correlations; b) Theil-Sen slopes; and c)
428 the PW mean difference for high AOD events. In addition to the three scatterplot comparisons, all locations for which
429 for the sign of the AOD and PW relationships differed between the AERONET and the NAAPS-RA datasets were
430 identified. For these identified sites, the distribution of AERONET correlations are plotted by season in Figure 9d.
431 This is included as a means to examine the strength of the observed AOD/PW relationship under conditions when the
432 datasets disagree. Overall, the observations and model are in general agreement in the sign of the correlations (Figure
433 9a) with similar results found for the Theil-Sen slope and the PW mean differences for high AOD events (Figure 9b,c).
434 Differences in the sign of the correlation are found for 15.5, 9.5, 10.2, 10.1% of [analyzed/analysed](#) AERONET sites
435 for the DJF, MAM, JJA, and SON months, respectively. For all seasons except JJA, these differences are mostly
436 associated with a negative correlation in the AERONET data and a positive value in the NAAPS-RA. Differences in
437 correlation sign occur for sites in which the AERONET-generated correlations are weak, mostly falling below 0.20
438 (Figure 9d), with the exception of the Jomsom AERONET site in JJA in which AERONET indicated a strong negative
439 correlation and the reanalysis had a slight positive, but statistically insignificant relationship as previously discussed.
440 For the strongest correlation sites, AERONET and NAAPS are in good agreement in DJF and MAM (Tables 1 and
441 2). For JJA and SON, NAAPS-RA has a tendency to produce weaker correlations relative to AERONET (Tables 3
442 and 4). Some differences are expected given that the event sampling is different between the AERONET observations
443 and the 16-year NAAPS-RA. However, the overall agreement in the correlations between the two datasets provides
444 some confidence in the NAAPS-RA for generating regionally and seasonally varying AOD and PW relationships on
445 a global scale.

446 3.3 Slope Evaluation

447 With the consistency between AERONET and NAAPS-RA established, a more thorough evaluation of the strength of
448 the slope of AOD-PW relationship has been conducted. As previously discussed, the AOD and PW relationship in
449 both the AERONET and NAAPS-RA datasets were quantified using a Theil-Sen regression in order to fit a slope to
450 the change in AOD per unit cm PW (Figures 7 and 8). Examples of NAAPS-RA and AERONET Theil-Sen fittings
451 for eight AERONET sites scattered over the globe, each with their own unique aerosol environment are shown in
452 Figure 10. Included are positive and negative correlation examples shown for each season (DJF: Beijing China and
453 Lamto, Ivory Coast; MAM-Houston Texas and Ilorin Nigeria; JJA-Helsinki, Finland and Dakar Senegal; and SON-
454 Dhadnah UAE and Palangkaraya, Indonesia) with the selected sites having some of the strongest correlations for the
455 respective seasons in the AERONET and NAAPS-RA datasets (Tables 1-4). Good agreement is shown between the
456 NAAPS-RA and AERONET-generated Theil-Sen slopes at the selected sites with the largest differences occurring at
457 the Lamto and Palangkaraya sites in which relatively less AERONET observations are available. These fittings are
458 calculated for each grid and AERONET site and are used to generate the results in Figures 7 and 8. The examples in
459 Figure 10 show the insensitivity of the Theil-Sen regression to outliers, while the correlation coefficient is quite
460 sensitive to such values. Beijing in DJF exhibits a large change in AOD with PW, as high AOD events are more
461 frequent at this location (Figures 5 and 10). However, places like Houston, Helsinki and Dhadnah have relatively
462 smaller Theil-Sen slopes as high AOD events, with a value around 1, occur less frequently and do not influence the
463 slope. For these locations, the range of frequently observed AOD events is much smaller (Figures 5 and 10), resulting
464 in small changes in AOD with PW. Although there is certainly scatter in the data points in Figure 10, statistically
465 significant trends exist. The scatter in the data points occurs more so at negative correlation locations (Figure 10),
466 resulting in smaller correlation coefficients. While the relationships for both positive and negatively correlated
467 locations are statistically significant and the Theil-Sen regression gives an overall trend, the scatter indicates
468 differences in AOD and PW relationships will occur from day to day. This is expected as the AOD-PW relationship
469 is based on a combination of transport covariance and local meteorology-source relationships.

470 The global and seasonal pattern in the positive and negative Theil-Sen slopes are consistent with the correlation
471 analysis results (Figures 7 and 8). The biggest Theil-Sen slopes tend to occur where larger IQR ranges are present
472 (Figure 5), as was shown for the Beijing Theil-Sen slope example in Figure 10. The largest slopes in both datasets are
473 centered on Beijing in the DJF months with values exceeding 1cm^{-1} . Beijing consistently has some of the largest
474 positive changes in AOD with PW in the AERONET dataset for all seasons with values, including 95% confidence
475 intervals, of $1.1(1.0-1.2)$, $0.35(0.32-0.38)$, $0.46(0.43-0.51)$, and $0.26(0.22-0.3)$ cm^{-1} for DJF, MAM, JJA, and SON,
476 respectively. The NAAPS-RA is largely consistent with AERONET for the DJF and MAM months with corresponding
477 values of $1.13(1.08-1.18)$, and $0.31(0.29-0.33)$ cm^{-1} . Less sensitivity to PW is found in the reanalysis for JJA and
478 SON with corresponding values at Beijing of $0.13(0.11-0.14)$, and $0.18(0.17-0.20)$ cm^{-1} . This is likely due to an
479 underestimation of haze formation within NAAPS, as with other global models (e.g., Sessions et al., 2015; Xian et al.,
480 2019) and also possibly due to the underestimation of AOD in summer from NAAPS due to a low AOD bias in the
481 assimilated satellite AOD datasets in the East Asia region (Eck et al., 2018). Large positive changes in AOD with PW
482 extend through Asia, the Middle East, and Northern Africa, all regions impacted by high AOD events. As is the case

483 in the correlation results, the strong dipole in slopes is clear over North Africa with positive slopes to the North and
484 negative slopes in the southern Sahel region. Likewise, negative slopes are mainly associated with burning regions
485 with the exception of Southern Africa in JJA. Statistically significant correlations and slopes at high latitudes,
486 particularly Antarctica, indicate aerosol/water vapor transport in the model since local sources are limited, although
487 AOD and PW values are low (Figures 5 and 6).

488 Recall the scatterplot comparison of AERONET and NAAPS generated changes in AOD with PW is shown in Figure
489 9(b). Again, there is generally good agreement between the datasets, consistent with the correlation comparison. The
490 signs of the slopes are the same with the exception of 14.6, 9.2, 12.3, and 8.1% of sites for DJF, MAM, JJA, and SON,
491 respectively. Sites where differences in sign are observed have weak correlations (Figure 8d). The NAAPS-RA has a
492 tendency to under-predict negative changes in AOD with PW relative to AERONET for SON months where peak
493 negative slopes are generated from AERONET. This is also shown in Table 4 as well as the global maps in Figure 7
494 where differences can be seen, particularly in the Sahel and Southeast Asia. At the Kuching site in Borneo in SON,
495 the AERONET generated slope is $-0.37(-0.48 \text{ to } -0.28)$ cm^{-1} with a reanalysis value of $-0.11(-0.13 \text{ to } -0.09)$ cm^{-1}
496 likely due to strong mesoscale variability and poor constraint in biomass burning on Borneo (Reid et al., 2013; Wang
497 et al., 2013). Additionally, this could again be due to satellite retrieval screening of smoke as cloud and NAAPS failing
498 to simulate the highest AOD smoke events in Borneo, especially in the dry El Nino years such as 2015 (Eck et al.
499 2019, Shi et al. 2019). The reanalysis also tends to under predict positive slopes for JJA at the AERONET sites where
500 the largest slopes are observed. This difference is not restricted to a particular region, but can be seen in East Asia,
501 Africa, and Mexico City (Figure 7). As an example, the Tamanrasset site in Algeria exhibits slopes in the AERONET
502 data of $0.26(0.23-0.30)$ cm^{-1} and in the reanalysis of $0.07(0.06-0.08)$. Likewise, at the Lubango site in Angola, the
503 slope is $0.27(0.21-0.34)$ cm^{-1} in the AERONET data and $0.13(0.12-0.14)$ cm^{-1} in the reanalysis. The Tamanrasset
504 site is at 1377 meters altitude in the Ahaggar Mountains which is significantly higher than the surrounding terrain in
505 the Saharan Desert. The Lubango site in Angola is at 2047 meters, also higher than a portion of the surrounding terrain.
506 This terrain/altitude influence is likely a factor in the discrepancies. The differences in slopes for JJA are also shown
507 in Table 3.

508 **3.4 Evaluation of the AOD and PW Probability Distribution**

509 While the correlation and slope evaluation is used to define a seasonal AOD and PW relationship across the datasets,
510 it is expected that variations in the aerosol and water vapor relationship will exist across air masses. As a result, a
511 probability distribution evaluation is another useful way to examine the data. The seasonal evaluation of the probability
512 distributions is included in Figure 7, ~~below-next to~~ the correlation and slope results. The plots show the statistically
513 significant difference in the mean for the PW distribution associated with high AOD events (AOD values more than
514 1 standard deviation above the mean) and the full PW distribution. Red regions/sites indicate that the PW mean for
515 high AOD events is statistically higher than the full distribution mean (i.e. higher moisture levels). Blue regions/sites
516 indicate a lower PW mean for high AOD events (i.e. dryer conditions). Regions or sites in white have no statistically
517 significant difference. The spatial pattern in the probability distribution evaluation are similar to the correlation and
518 slope analysis, however, the probability distribution evaluation highlights different regions than the previous analyses.

519 For example, across all seasons, larger changes in PW for high AOD events are observed in Argentina, South America,
520 including at the CEILAP-BA (Buenos Aires, Argentina) with values of 0.88, 0.94, 1.01, and 1.00 cm for DJF, MAM,
521 JJA, SON in the AERONET dataset and values of 0.61, 0.35, 0.95, and 0.73 cm in the NAAPS-RA dataset. This is a
522 region that is impacted by both local pollution and transported biomass burning (Resquin et al. 2018). Larger changes
523 in PW for high AOD events are also observed over Northern Australia during MAM, which is consistent with peak
524 bushfire season in the region. Larger changes in PW are also found over the United States and Canada, consistent with
525 patterns in the correlation evaluation, but with more pronounced values relative to other locations. ABF is generally
526 the dominant aerosol type with biomass burning from Central America and Western US/Boreal Regions during the
527 MAM and JJA seasons, respectively. Likewise, Eurasian Boreal regions associated with biomass burning activity
528 during JJA are more pronounced in the PW distribution evaluation. The peak in values in the Southeast United States
529 are found during the DJF season. During MAM and SON, the peak areas include most of the Eastern United States
530 and extending into Canada and Central America. However, regions that were more pronounced in the correlation and
531 slope evaluation, have smaller differences in mean PW for high AOD events, Beijing being a good example of this.
532 Based on AERONET, the difference in mean PW at Beijing is 0.21cm while the difference is 0.35cm in the NAAPS-
533 RA for DJF when the strongest correlations and largest slopes were found. However, sites like Stennis, Mississippi
534 (Table 1) which had a much smaller slope than Beijing (0.04cm-1 compared to 1.1cm-1) have a much larger difference
535 in mean PW with the AERONET value of 1.08cm and the NAAPS value of 1.16cm. This is because the probability
536 distribution evaluation is taking into account those infrequent, outlier events that don't affect the Theil-Sen slopes.
537 Locations where the IQR is relatively small, such as the United States, Europe, Australia, and parts of South America
538 and Southern Africa have greater differences in mean PW, despite having small Theil-Sen slopes, due to the impact
539 of outlier events. For many of these regions, the outliers are associated with biomass burning, indicating that PW is a
540 useful tracer for such events.

541 Like the correlation and slope evaluation, a comparison of AERONET and NAAPS generated differences in mean
542 PW was conducted by season. Similar to the previous two comparisons, AERONET and NAAPS are in agreement in
543 the sign of PW difference for most locations, demonstrated by the global plots in Figure 7 and the scatterplots in
544 Figure 8c. The % of sites that have differences in sign between the two datasets are 8.9, 6.87, 5.86, and 4.15% for
545 DJF, MAM, JJA, and SON, respectively. These percentages are smaller than the % of sites with differences in the
546 correlation and slope analysis. However, like the previous evaluations, most sites that exhibit sign differences between
547 AERONET and NAAPS had weak AOD and PW relationships ($R < 0.20$, Figure 8d), with the exception of some
548 outliers in which small scale features that cannot be resolved in the global model may be at play. The comparisons
549 between AERONET and NAAPS-RA across the different evaluations indicate that NAAPS is generating AOD and
550 PW relationships that are pretty consistent with the observational data. Although differences in magnitude are present,
551 the direction of the relationships are very consistent, providing confidence in the use of the NAAPS-RA for further
552 exploring the AOD and PW relationship, particularly in the vertical and accounting for hygroscopic affects.

553 3.5 Vertical Evaluation of the AOD and PW Relationship

554 In addition to calculating the full column-integrated AOD and PW correlations in the NAAPS-RA, the correlations
555 were also evaluated by vertically integrating the extinction and specific humidity through previously defined pressure
556 levels in the atmosphere that correspond to a boundary layer, lower, middle, and upper free troposphere. This
557 evaluation was conducted seasonally, like the fully integrated analysis, with results shown in Figure 11. In addition to
558 the global plots, histograms of the AOD and PW correlations for the full column and the vertical components of the
559 atmosphere are shown in Figure 12. It is notable that stronger positive correlations exist when looking at limited parts
560 of the atmosphere compared to the fully integrated column. This is most evident in the global plots for ocean regions,
561 particularly in the Southern Hemisphere, where correlations exceeding 0.5 occur compared to the fully integrated
562 correlations that are on the order of 0.2. This result is not unexpected given that the vertical components of the
563 atmosphere look different depending on things like vertical mixing, a local aerosol and water vapor source compared
564 to a long-range transport event, the relative humidity profile etc. Additionally, some regions exhibit stronger
565 correlations in certain portions of the atmosphere. For example, dust dominated regions such as the Sahara, Arabian
566 Peninsula and the Gobi and Taklimakan deserts have the strongest correlations in the mid FT. This is higher up in the
567 atmosphere than expected, given for example, studies have shown East Asian dust heights to range from 1.9 to 3.1km
568 (Liu et al. 2019) and the typical description of the Saharan Air Layer (SAL) includes dust-laden air between
569 approximately 850 and 500 hPa (Karyampudi et al. 1999) with several other studies identifying Saharan dust up to
570 ~5km for summertime dust transport (Mortier et al. 2016, Veselovskii et al. 2016, Tesche et al. 2011). This indicates
571 that the model may be transporting too much dust aerosol and water vapor higher into the atmosphere and this transport
572 is well correlated. Correlations over North America and Eastern Europe are strongest in the BL to lower FT.
573 Wintertime correlations over East Asia/Beijing are pretty consistent throughout the column. Negative correlation
574 regions associated with smoke aerosol, including the Sahel, Southern Africa, and Southeast Asia have the strongest
575 correlations in the lower FT and largely disappear beyond this point. The shift in correlations with vertical location
576 are also evident in the histograms (Figure 12) when compared to the full column distribution. This is particularly the
577 case for the lower and mid free troposphere where the number of grids with correlations greater than 0.5 increase.
578 Additionally, the shift of the correlations to mostly positive can be seen in the mid and upper free troposphere
579 histograms.

580 **3.6 Impact of Hygroscopic Growth on AOD and PW relationships**

581 The final consideration in this work is hygroscopicity. Although the effects of clouds on the AOD and PW relationship
582 is also important to understand, this effect cannot be investigated using NAAPS since the model does not account for
583 the processing of aerosol in cloud droplet, rapid gas-to-particle conversion in cloud droplets or the high RH halo in
584 the immediate vicinity of clouds. However, this should be considered in follow-on work. While relationships between
585 AOD and PW have been demonstrated, this signal can be either from co-transport or a confounding relationship
586 between enhanced PW and RH. The correlation between RH and PW is shown in Figure 13 by season and for the
587 boundary layer and parts of the free troposphere. The largest spatial variations in the PW and RH correlation occur in
588 the boundary layer, as anticipated, with strong correlations found over Africa, extending into the Indian Ocean/India,
589 located further North during JJA and further South during DJF and similar patterns during MAM and SON. Other
590 regions of high correlation in the boundary layer include off the coast of South America, parts of Australia, and limited

591 locations in the tropical oceans. Beyond the boundary layer, the overall patterns are generally consistent throughout
592 the vertical column with strong correlations in the subtropics and tropics (>0.9) with some variations on the extent by
593 season. In JJA for example, this high correlation region extends further north while in DJF the high correlation region
594 extends further in the Southern hemisphere. In this highly correlated region, hygroscopic growth is expected to be a
595 significant driver in AOD and PW relationships when dust is not the dominant aerosol type. RH and PW correlations
596 are higher over ocean regions than over land in the northern hemisphere, which should be impactful for sea salt aerosol
597 and PW correlations. The impact of the RH and PW correlations on the AOD and PW relationship are shown in
598 calculated seasonal relationships between “dry” AOD, which excludes the impact of hygroscopic growth, and PW in
599 the NAAPS-RA in Figure 14. This figure includes the correlations, the slope of the “dry” AOD and PW relationship,
600 and the statistically significant difference in mean PW for high “dry” AOD events. The removal of hygroscopic growth
601 from the AOD calculation had the following outcomes on the resulting correlations: 1) the previously positive
602 correlation was reduced in magnitude 2) the previously negative correlation coefficient became more negative 3) the
603 sign of the correlation flipped from positive to negative and 4) little to no change in the correlation. Regions such as
604 the Eastern United States and Europe fall into the first category where positive AOD and PW correlations are found
605 for all seasons, but the correlation coefficient is greatly reduced. For the Eastern United States, peak correlation
606 coefficients were in the approximately 0.6-0.7 range with hygroscopic growth and fell below 0.5 without it. This is
607 especially true in JJA when RH and PW correlations are the strongest. Likewise, positive correlations in Europe are
608 still present, but weakened. In these cases, hygroscopic growth amplifies an existing positive relationship that is
609 somewhat weak when evaluating seasonal data by correlation. In regards to the second category, this corresponds to
610 regions dominated by smoke aerosol that previously exhibited negative AOD and PW relationships, such as Peninsular
611 Southeast Asia during the MAM months and Insular Southeast Asia during the SON months. Additionally, increases
612 in negative correlations are found for aerosol transport from Asia across the Pacific Ocean. In these cases, hygroscopic
613 growth reduces an existing negative relationship between aerosol and water vapor. Ocean regions mostly account for
614 the third category where the correlation flipped from a weak positive to negative value. Regions that are dominated
615 by dust, including the Sahara and Arabian Peninsula, fell into the fourth category as there is no hygroscopic growth
616 for dust in NAAPS.

617
618 In regards to the slope of “dry” AOD and PW, the same categories apply with similar spatial patterns relative to the
619 correlation analysis. Additionally, the same is true when examining the difference in mean PW for high “dry” AOD
620 cases. In this case, it is found that either: 1) an increase in PW is still statistically significant, but the difference in
621 mean PW is much less 2) a decrease in PW for high “dry” AOD cases is still statistically significant with a larger
622 decrease when not considering hygroscopic growth 3) the sign of the difference flipped from an increase in PW to a
623 decrease or the difference became statistically insignificant and 4) the PW difference did not change much due to dust
624 dominated conditions. While the modeled differences in PW are statistically significant when excluding hygroscopic
625 growth, they are small, with peak differences on the order of a few millimeters. The results here indicate that
626 hygroscopic growth of aerosol plays an important role in the AOD and PW relationship. While PW is still a good
627 tracer for AOD as shown in this work, it should be kept in mind that there is a difference in water vapor as a tracer for

628 AOD and for aerosol mass. It is expected that the relationship between “dry” AOD and PW would be a closer
629 representation of the dry aerosol mass to PW relationship.

630 **3.7 Discussion through Example Cases at Individual AERONET Sites**

631 In order to further understand regional differences in observed AOD and PW relationships, individual sites in which
632 strong AOD and PW relationships were identified and had several years of observational data available were selected
633 for further analysis. These sites included: 1) Tallahassee, Florida for Southeast US pollution (Figure 15); 2) Beijing,
634 China for Asian haze and dust (Figure 16); 3) Izana, Canary Islands for Saharan dust (Figure 17); and Alta Floresta,
635 Brazil for South American biomass burning (Figure 18). For the four identified AERONET sites, the daily-averaged
636 AOD and PW timeseries are examined for seasons in which correlations were found to be strong. This includes DJF
637 for the Tallahassee and Beijing sites and JJA for Izana. At these sites, the identified relationships between AOD and
638 PW were positive. The Alta Floresta site, which exhibited negative AOD and PW relationships in the presented results,
639 is further examined for the SON biomass burning season. The daily-averaged data are included since this is what was
640 analyzed in the previous analyses. Additionally, the AERONET data, without any averaging, is further examined for
641 individual cases from the site-specific timeseries for which peaks in AOD and/or PW were found. NAAPS-RA AOD
642 and PW fields are also shown for the selected cases (Figures 15-18).

643 At the Tallahassee site, the predominant aerosol type is ABF/pollution and although AOD values are generally low
644 during DJF (mean values in the 0.1-0.2 range, Figure 3), strong AOD and PW relationships were found with
645 correlations of 0.74 in the AERONET dataset and 0.66 in the NAAPS-RA with PW mean differences around 1cm for
646 high AOD events (Table 1). The daily-averaged AOD and PW timeseries for the 2018-2019 DJF season are shown in
647 Figure 15a. The timeseries indicates, consistent with the correlation analysis, that the daily-average AOD and PW
648 generally move together. There are several joint peaks in AOD and PW that occur during the time period and three
649 selected cases are examined further, including 1/1/2019, 2/7/2019, and 2/17/2019, with these events identified in the
650 Figure 15a timeseries using red arrows. The AERONET AOD and PW timeseries for these three cases are shown in
651 Figures 15b-d, respectively. The 2/17 case has the least data points available, making it harder to evaluate diurnal
652 changes in AOD and PW, however, the 1/1 and 2/7 cases have a good number of data points throughout the afternoon
653 and later into the evening. For these two cases in particular, the changes in AOD and PW throughout the day are
654 generally consistent with each other, indicating that the AOD and PW relationships can extend to sub-daily timescales.
655 AOD and PW plots for the three identified cases are shown from the NAAPS-RA in Figure 15e as a means to assess
656 the types of aerosol events that are impacting Tallahassee when coordinated peaks in AOD and PW are observed. For
657 all three cases, coincident transport of AOD and PW is observed in the reanalysis fields, associated with a frontal
658 system. This type of frontal transport was commonly found for events in which coincident PW and AOD peaks are
659 observed at Tallahassee. As the DJF season in the Southeast United States has significant frontal activity, this is likely
660 an important factor in enhanced AOD/PW relationships during this season.

661 Beijing is an urban site that commonly experiences high AOD levels related to pollution as well as transported dust
662 and smoke events. Wintertime events are notorious for exhibiting some of the worst air quality in the world for a major
663 population center (e.g., Wang et al., 2014; Gao et al., 2016; Zhang et al., 2018). Additionally, Beijing has the benefit

664 of a long AERONET data record with measurements dating back to 2001. Like Tallahassee, the AOD and PW
665 timeseries at Beijing is evaluated for the 2018-2019 DJF season (Figure 16) with strong positive relationships
666 identified in both the AERONET and NAAPS datasets with correlations of 0.71 and 0.76, respectively, and the change
667 in AOD with PW exceeding 1cm^{-1} (Table 1). As indicated in Figure 4, ABF/pollution is the dominant aerosol type
668 with some dust present with much higher AOD values observed at this location (Figures 3 and 5). In East Asia,
669 pollution build-up often occurs under stagnant weather conditions where a stable atmosphere leads to limited vertical
670 mixing (Wang et al. 2014, Li et al. 2019) with the monsoon being an important factor in determining synoptic
671 conditions. In particular, the East Asian Winter Monsoon (EAWM) has been shown to be a controlling factor in aerosol
672 concentrations during the winter season (Li et al. 2016; Jeong et al. 2017). With a strong EAWM, reduced aerosol
673 concentration occur over northern East Asia, including Beijing, due to stronger northerly winds. In weaker EAWM
674 years, increased aerosol concentrations occur in the north due to weakened winds and more stagnant conditions. The
675 daily-averaged AERONET AOD and PW timeseries for 2018-2019 DJF is shown in Figure 16a. Consistent with the
676 previously presented evaluations, the daily-average time series for this particular DJF time period are well correlated
677 with AOD and PW moving up and down together. As was done for the Tallahassee site, several peaks in AOD and
678 PW were selected for further evaluation and are highlighted with red arrows on Figure 16a, including the peak on 1/3
679 and its subsequent decrease on 1/4/19, and the peak on 12/20/18 and its subsequent decrease on 12/21/18. The non-
680 averaged AERONET AOD and PW timeseries for these two cases are shown in Figure 16b and c, respectively, with
681 a zoomed in view of 12/21 on Figure 16d. For both of these events, high AOD from ABF/pollution and PW values
682 are observed with a subsequent dropoff the following day, which are well coordinated in the full dataset. The closer
683 look at the data on 12/21/18 (16d), like the previous Tallahassee examples, shows consistent movement between the
684 measured AOD and PW indicating the presence of correlations on short timescales. For both of these events, the
685 NAAPS-RA AOD and PW fields are shown for both the peak and subsequent dropoff in Figure 16e. The movement
686 of the large-scale air mass can be seen in both the AOD and PW fields. For the 1/3/19-1/4/19 event, NAVGEM
687 meteorological fields indicate weakened northerly winds due to a region of high pressure over the eastern portion of
688 the continent, leading to stagnant conditions at the surface in Beijing and local pollution and water vapor build-up. On
689 the following day, the high pressure system moved eastward. As a result, the Siberian High northerlies were no longer
690 suppressed and a more typical wintertime circulation resumes with the winds jointly pushing the aerosol and water
691 vapor southward and away from Beijing. For the 12/20/18-12/21/18 case, extensive multi-level cloud cover can be
692 seen in both MODIS Terra and Aqua images on 12/20, indicating that this may be a case where clouds may have
693 played a role in gas-to-particle conversion in the polluted air and/or enhanced particle humidification in the high RH
694 fields associated the clouds, consistent with the findings of Eck et al. (2018). As the air mass moves on 12/21, a joint
695 reduction in both AOD and PW is observed at Beijing, demonstrating the impact of large scale transport. Thus in the
696 Beijing case, the overall regional weather patterns are an important factor in the AOD and PW relationship.

697
698 The third site that is examined is Izana in the Canary Islands (Figure 17). The Izana site, which is located
699 approximately 300km west of the African coast, is particularly useful for evaluating aerosol and water vapor
700 relationships for free tropospheric dust. It has also been noted in the community that against a Saharan air layer free

701 subsidence regime, the infrared signals of Saharan Air Layer dust are quite small relative to co-transported water vapor
702 (Gutleben et al., 2019; Ryder, 2021; Barreto et al., 2022). Nevertheless, forecasters find the water vapor signal useful
703 in tracking dust events (Kuciauskas et al., 2018). Izana is a mountain site located at approximately 2400m, above a
704 strong subtropical temperature inversion layer which makes it ideal for monitoring free tropospheric plumes. In the
705 summer months, frequent and intense Saharan air mass outbreaks in the subtropical free troposphere impact the site.
706 Particularly large AOD dust storms were observed transporting Saharan dust across the Atlantic in the summer of
707 2020, including the so called “Godzilla” dust event in June that has been examined in detail in previous studies (Francis
708 et al. 2020). As a result, this time period was evaluated in further detail at Izana with a focus on several dust events.
709 In the analysis conducted in this work, positive relationships between AOD and PW were found in both the AERONET
710 and NAAPS datasets at Izana during the JJA season with the AERONET dataset having a correlation of 0.66 and the
711 NAAPS-RA indicating a weaker correlation of 0.48 (Table 3). As noted for other sites, this difference may be due to
712 altitude effects at the Izana site which may not be captured in NAAPS. The daily-average AOD and PW timeseries
713 for the 2020 JJA season at Izana are shown in Figure 17a. The AOD and PW are pretty well correlated, although there
714 are PW peaks present without the presence of aerosol. As sources of aerosol and water vapor are different, this is not
715 unexpected. Three of the peak from the timeseries as indicated by the red arrows were selected for further evaluation,
716 including 6/14/20, 7/18/20, and 7/31/20 with timeseries shown in Figures 17b-d, respectively. As was shown for the
717 previous pollution cases, the AOD and PW are well correlated in the non-averaged dataset showing the presence of
718 correlations for dust events on timescales less than a day. The NAAPS-RA AOD and PW fields are shown for the
719 6/14/20 case in addition to the associated dropoff of both AOD and PW on 6/18/20, as well as for the 7/18/20 and
720 7/31/20 events in Figure 17e. For the 6/14/20 case, CALIPSO indicates dust tops near Izana at around 5km. A cutoff
721 low was present to the northwest of Africa and a subtropical high over the Western coast of Africa which resulted in
722 increased dust generation and recirculation. The southwesterly winds transport the dust to Izana on June 14 and at the
723 same time, moist ocean air shown by the PW fields is transported to Izana as well, resulting in a spike in both AOD
724 and PW at the AERONET site. On June 18, the moisture and dust begin pushing south and west across the Atlantic,
725 resulting in decreases in AOD and PW at the same time at Izana. Similar examples of dust and water vapor cotransport
726 are shown for the 7/18/20 and 7/31/20 cases. These results are consistent with previous studies which have indicated
727 enhanced water vapor mixing ratios associated with the dust in Saharan Air Layer events (Marshall et al. 2008, Jung
728 et al. 2013, Kanitz et al. 2014). Thus, Izana is a good example of subtropical free tropospheric co-transport of water
729 vapor and dust.

730
731 The final site evaluated was Alta Floresta, Brazil for the 2019 SON season, when biomass burning is the dominant
732 aerosol type. Here, there is a strong seasonal dependency: drier seasonal conditions are associated with a July-October
733 biomass burning season. At this site and other regions of biomass burning, negative correlations between AOD and
734 PW were identified in the presented evaluations. For Alta Floresta, SON correlations of -0.38 and -0.47 were
735 generated from the AERONET and NAAPS-RA datasets, respectively (Table 4). The daily-average AOD and PW
736 timeseries are shown in Figure 18a. An important thing to note about this timeseries is that a clear downward shift in
737 the PW fields occurs during October, consistent with monthly site climatologies from AERONET (3.61cm in

738 September, 4.15cm in October, 4.5cm in November). As fires are associated with dry conditions, the AOD fields
739 decrease as the water vapor increases. This shift towards wetter and decreased aerosol conditions is driving the
740 seasonal negative correlations for biomass burning regions. However, despite this overall shift, peaks in AOD and PW
741 are generally positively correlated. Several such cases are highlighted in the timeseries, including 9/15/19, and 9/23/19.
742 The 9/9/19 event is also highlighted in which the daily-averaged AOD peaks and the PW is at a low. For all three
743 cases, the AOD and PW timeseries shown in Figures b-d, show good positive correlations with AOD and PW changing
744 in the same way throughout the day. For the 9/9/19 case, this appears to a more locally driven event with the extent of
745 the smoke being more limited and the air being drier than the surrounding areas, suggesting a different air mass (Figure
746 18e). Additionally, there is much more small scale variability in the AOD and PW fields (Figure 18b). For this type
747 of event, the daily-average PW fields might not be as good of an indicator of what is going on with AOD. For the
748 other two cases, the NAAPS-RA plots indicate larger spatial extent of the smoke with more moisture associated with
749 the air mass. In this case, daily-average PW is a better indicator for large scale smoke events. However, for all three
750 smoke cases, AOD and PW are correlated on an event level. Thus, in this case the AOD-PW relationship identified in
751 the previously presented AERONET and NAAPS-RA evaluations represents the end of the burning season with wet
752 season onset in the middle of a “climatological season”. However, PW is a good positive indicator of AOD associated
753 with smoke on an event level, consistent with what has previously been shown in the literature for case study
754 evaluations.

755 4.0 Conclusions and Implications

756 The relationship between AOD and PW was evaluated globally ~~and-onat~~ seasonal and daily timescales using
757 approximately 20 years of AERONET observational data and the 16-year NAAPS-RA v1.0 model fields. As
758 AERONET observations have small measurement uncertainties, the observational analysis provides a best estimate
759 of the AOD and PW relationships. The observational analysis was combined with the NAAPS-RA in order to provide
760 a complete global perspective on the AOD and PW relationship as well as to provide an avenue for further exploration,
761 including what the likely drivers of these relationships are, what the relationships look like when taking the vertical
762 location into account, and the impact of hygroscopic growth on the AOD and PW correlations.

763 The major findings of this work include:

- 764 1. Seasonal relationships between AOD and PW are present across the globe at both seasonal and daily levels.
765 Most often AOD and PW relationships are strongly positive at seasonal to daily time scales, especially for
766 species such as pollution and dust. Biomass burning, however, has negative seasonal relationships due to fire
767 proclivity in dry seasons. Nevertheless, positive daily relationships are observed, associated with transport.
768 For regions like the Sahel, negative relationships between AOD and PW were found with spatial patterns
769 consistent with shifts in the ITCZ in which convection leads to aerosol scavenging.
- 770 2. Mid-latitude relationships between AOD and PW appear to be driven by frontal activity. While
771 tropical/subtropical relationships are driven by seasonal monsoon activity, ITCZ, and dry season patterns.

772 Dust transport associated with African easterly waves and cyclones are the link between aerosol and water
773 vapor for the Sahara.

- 774 3. The observed correlations between the AOD and PW were stronger when evaluated by vertical level with the
775 strongest correlations identified in the free troposphere, consistent with large scale aerosol and water vapor
776 transport. The location of the strongest correlations varied by aerosol type with dust dominated regions
777 having the strongest correlations in the mid free troposphere and smoke dominated regions having the
778 strongest correlations in the lower free troposphere.
- 779 4. Hygroscopic growth of aerosol particles, which is associated with increased relative humidity and often
780 occurs with increasing PW, has a large influence on the observed covariability between AOD and PW,
781 particularly in the mid-latitudes and for non-dust aerosol species. While transport covariance between AOD
782 and PW is present, the imbedded RH to PW relationship is the dominant term. This indicates that PW is a
783 good tracer for AOD, but not necessarily aerosol mass. [This finding has relevance for data assimilation](#)
784 [applications as well as PM retrievals.](#)
- 785 5. Covariability between AOD and PW for dust-dominated events is statistically significant and hygroscopic
786 growth is not an important factor.

787 Overall, this evaluation provides a global perspective on AOD and PW relationships. As has been previously
788 shown for individual case studies in the literature, this work reaffirms that PW is a useful tracer for aerosol
789 transport and such relationships are present across the globe. The seasonal AOD and PW evaluations conducted
790 in this work highlight regions and seasons for which AOD and PW relationships are expected to be more
791 prevalent. In particular, regions and seasons for which strong correlations and impacts on the PW distribution for
792 high AOD events are found are associated with synoptic scale aerosol events, including large-scale pollution and
793 smoke events over CONUS and Europe, Saharan dust events over the Atlantic, biomass burning events during
794 regional dry seasons in South/Central America, Africa, and Southeast Asia, and Asian dust/haze events. This is
795 confirmed when evaluating AOD and PW relationships on an event basis in different parts of the world in which
796 coincident peaks in daily-averaged AOD and PW were associated with large-scale aerosol transport events. The
797 vertical evaluation of the AOD and PW relationship provides further evidence that a strong contributor to the
798 identified relationship is synoptic scale aerosol transport in the free troposphere where the relationships were
799 found to be stronger than the fully integrated vertical column. These signals were present for all aerosol types
800 evaluated, indicating PW can be a useful tracer for AOD associated with all aerosol types as long as sources of
801 both and a common linking transport mechanism are present. For example, in the United States, fronts were the
802 linking transport mechanism while in East Asia, monsoonal patterns controlled joint transport. Likewise, dust
803 transport associated with African easterly waves and cyclones linked aerosol and water vapor for the Sahara.
804 Regions identified with strong correlations indicate the frequent presence of such synoptic scale co-transport
805 events while the PW distribution evaluation for high AOD events highlights regions in which such events are
806 present, but can be infrequent, as was the case for Boreal smoke events in summertime.

807 This work provides a first step in understanding the important aerosol and water vapor relationship on a global
808 scale. While aerosol and water vapor relationships will vary from air mass to air mass, this analysis provides an
809 understanding of where and when AOD and PW relationships are expected to be of importance and can be
810 exploited in 1) using water vapor as an aerosol tracer 2) in data assimilation applications and 3) for radiative
811 transfer studies in which collocated aerosol and water vapor can impact results. [These findings are also valuable](#)
812 [in identifying locations with potential for PM retrieval from space in which hygroscopic growth was found not to](#)
813 [be an important factor in the AOD and PW relationship.](#) While this analysis provides a quantitative estimate of
814 the aerosol and water vapor relationship in a big picture sense, the next step is to further understand the aerosol
815 and water vapor relationships on an event level. This is particularly important for data assimilation in which an
816 understanding of how this relationship temporally and spatially evolves for individual air masses needs to be
817 developed. As such, a follow-on study will be conducted to investigate the evolution of aerosol and water vapor
818 in space and time on an event level with a focus on specific regions identified in this work.

819 **Code and data availability**

820 AERONET observations are available for download through <https://aeronet.gsfc.nasa.gov/> and the NAAPS
821 reanalysis data in NetCDF format can be downloaded through The US Global Ocean Data Assimilation
822 Experiment (GODAE) server (<https://usgodae.org/>).

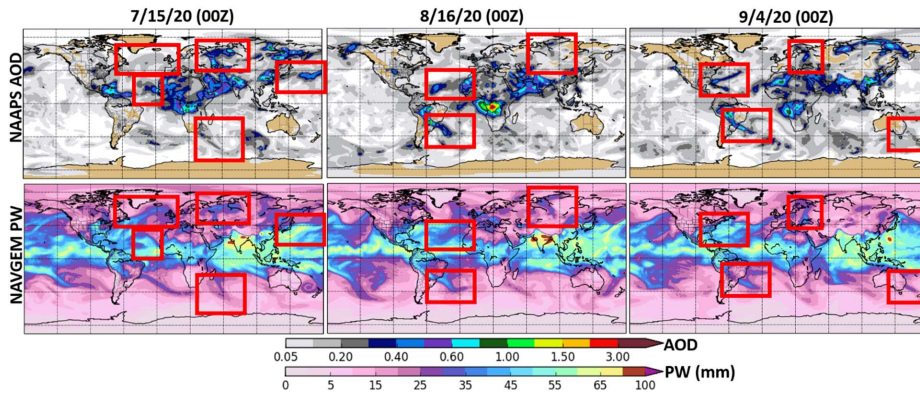
823 **Author contributions**

824 Authors Juli Rubin and Jeffrey Reid planned the analysis while Juli Rubin conducted the majority of the analyses
825 presented in this work. Peng Xian provided the NAAPS-RA dataset and provided help in using the data. Jeffrey
826 Reid, Juli Rubin, Christopher Selman and Thomas Eck helped in interpreting the results of the study with Chris
827 Selman focused on the meteorological aspect and Thomas Eck providing important feedback on the evaluation
828 using AERONET data.

829 **Competing interests**

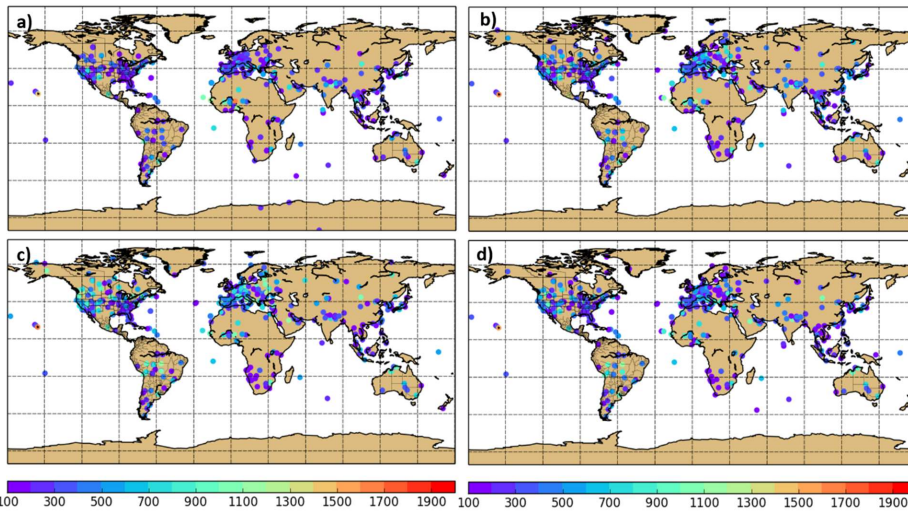
830 The peer-review process was guided by an independent editor, and the authors have no other competing interests
831 to declare.

832

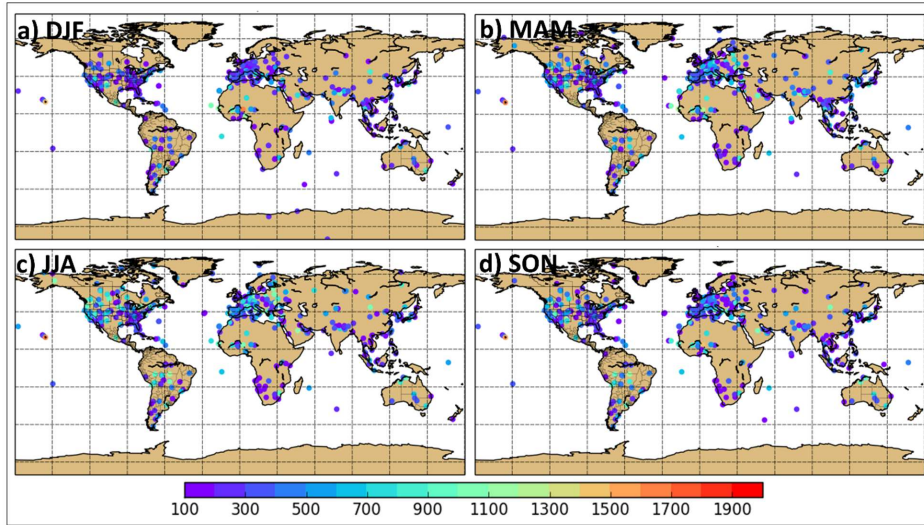


833

834 Figure 1. Examples of NAAPS AOD and NAVGEM PW forecasts in which similar synoptic scale transport patterns are
 835 found, particularly in the mid-latitudes. Aerosol and water vapor features with similar transport patterns are highlighted
 836 in matching red boxes in the AOD and PW plots. These types of co-transport events of both positive and negative correlation
 837 are found in forecasts on a daily basis.



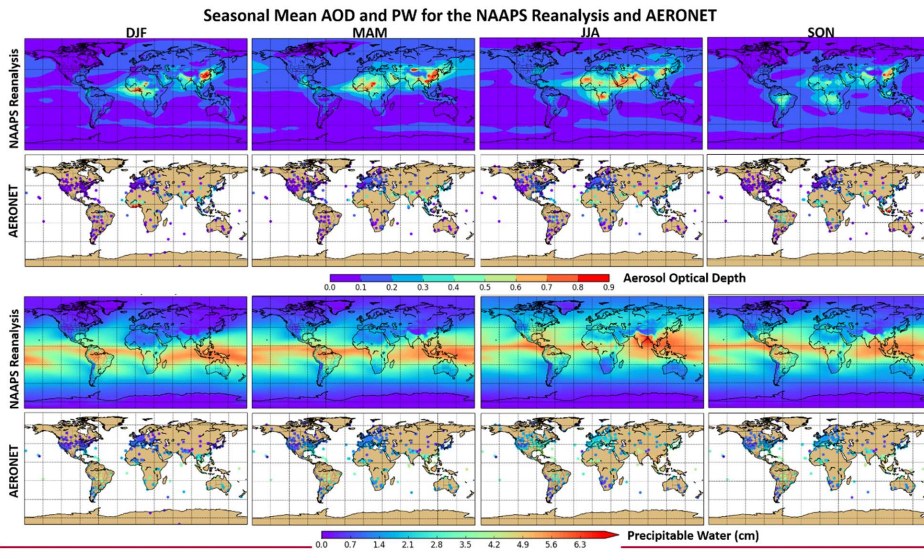
838



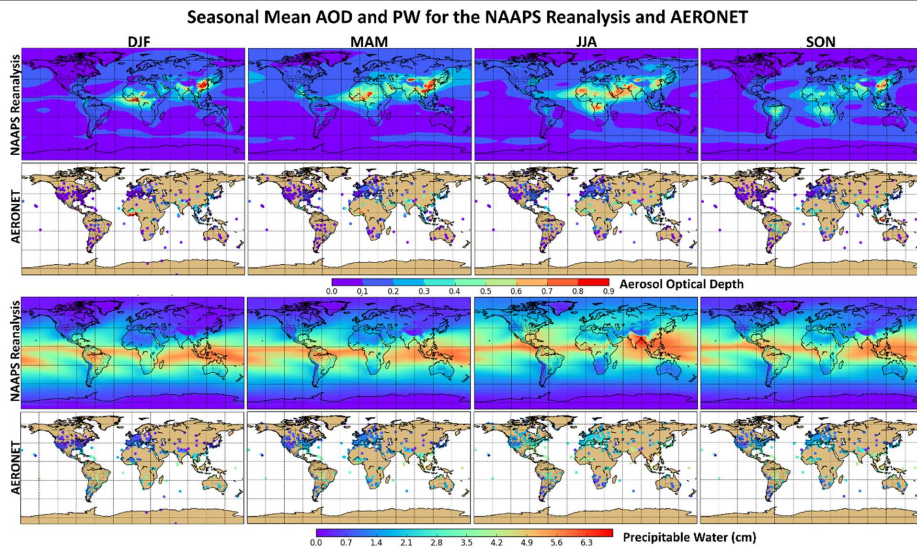
839
 840 Figure 2. Count of daily-averaged AERONET AOD and PW data points by season: a) DJF b) MAM c) JJA d) SON. Only
 841 sites with at least 100 points are shown.

842

843

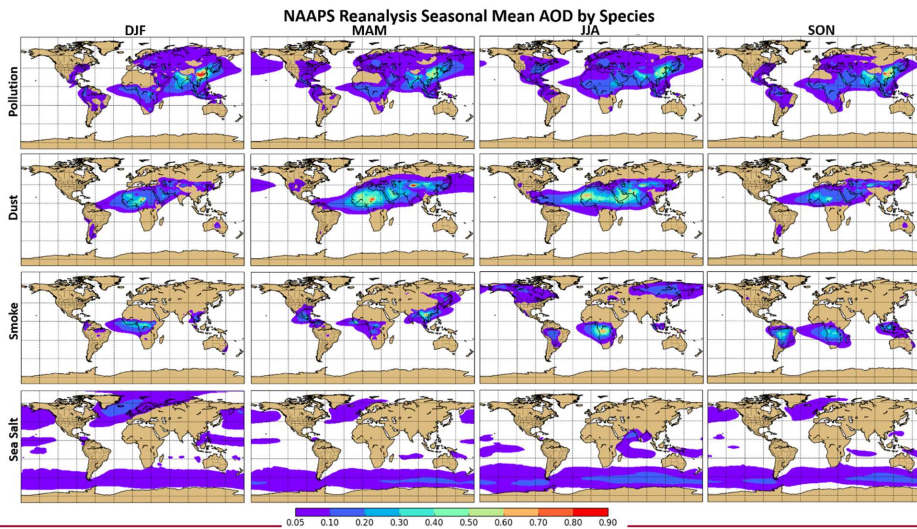


844

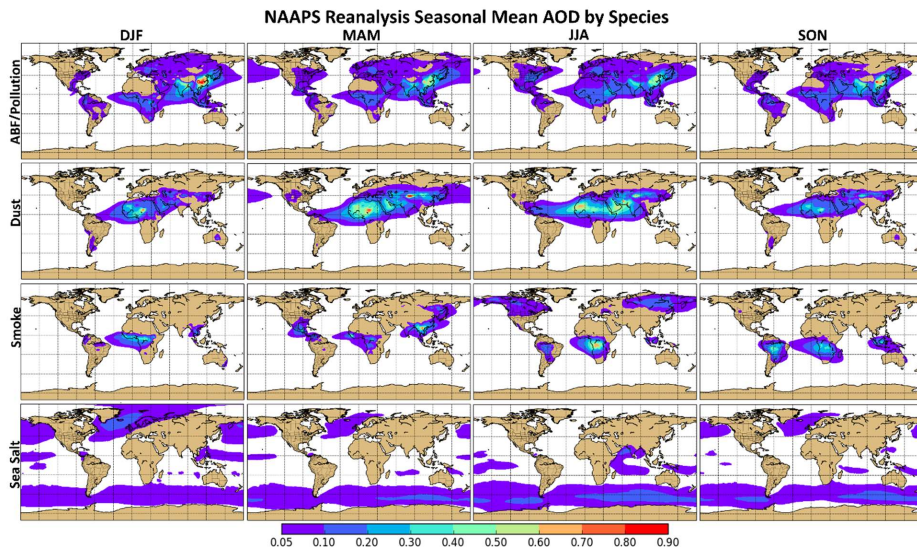


845

846 **Figure 3. Mean AOD and Precipitable Water (cm) for the NAAPS-RA and at AERONET sites by season: DJF, MAM, JJA,**
 847 **SON.**

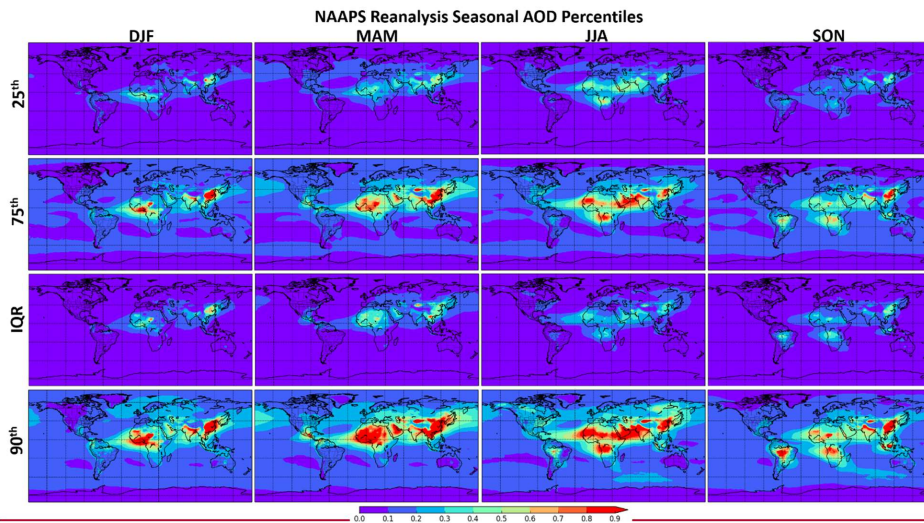


848

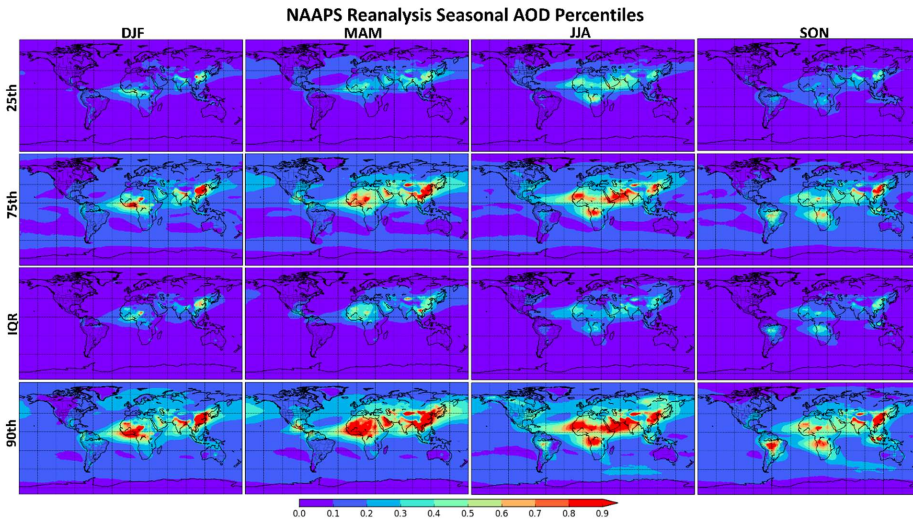


849

850 Figure 4. NAAPS-RA seasonally averaged AOD by aerosol type, including pollution (anthropogenic and biogenic fine
 851 aerosol), dust, smoke, and sea salt.

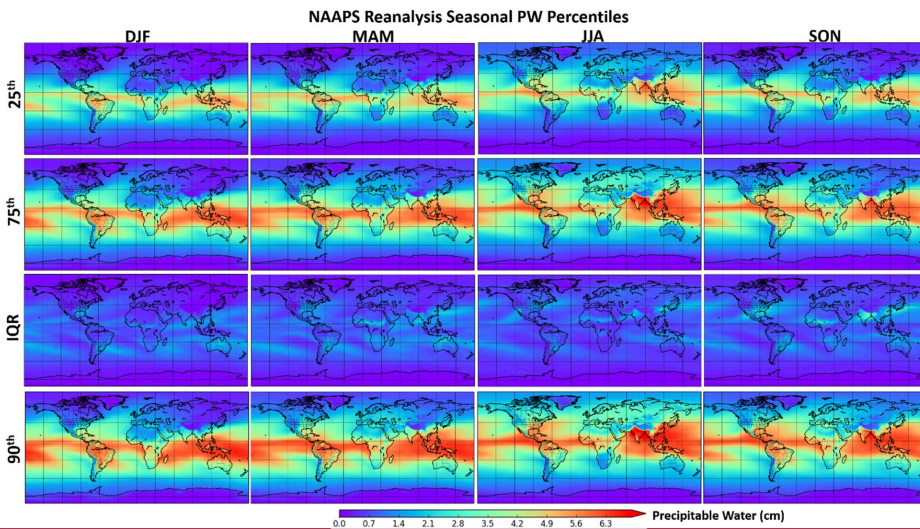


852

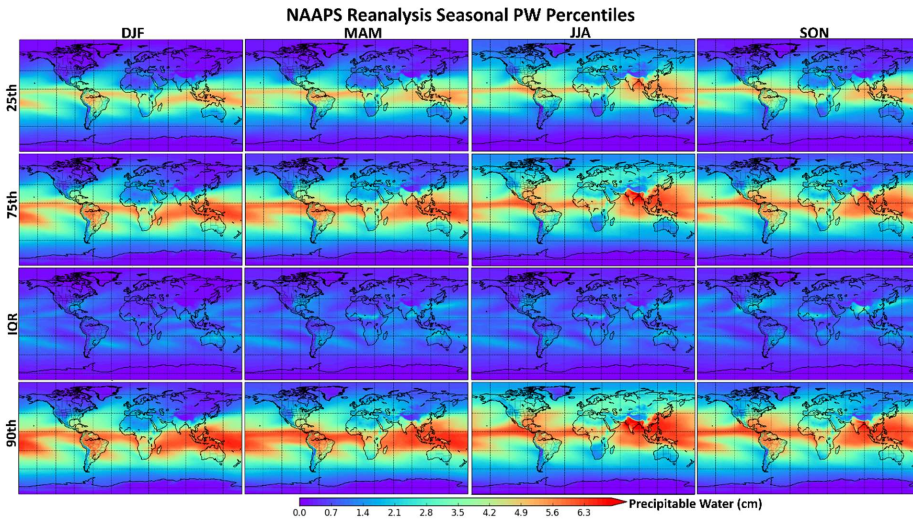


853
 854 Figure 5. NAAPS-RA AOD percentiles by season (DJF, MAM, JJA, SON). The 25th and 75th percentiles are shown along
 855 with the interquartile range (IQR). The 90th percentile is used to show high AOD values at a given location.

856

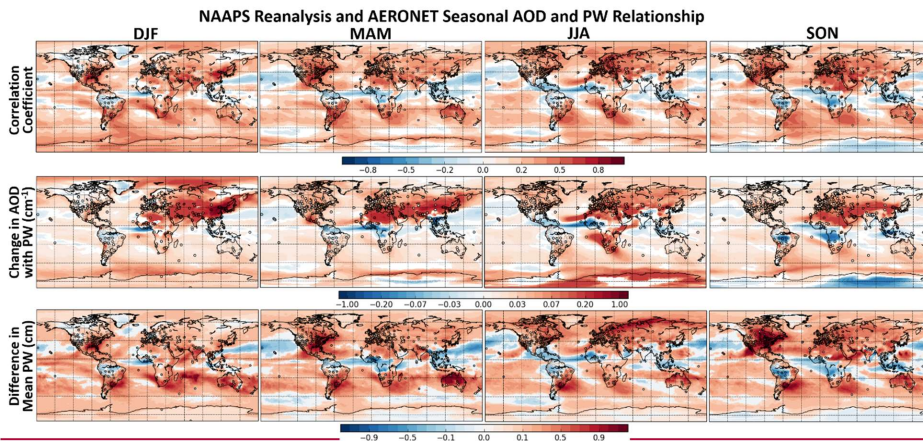


857

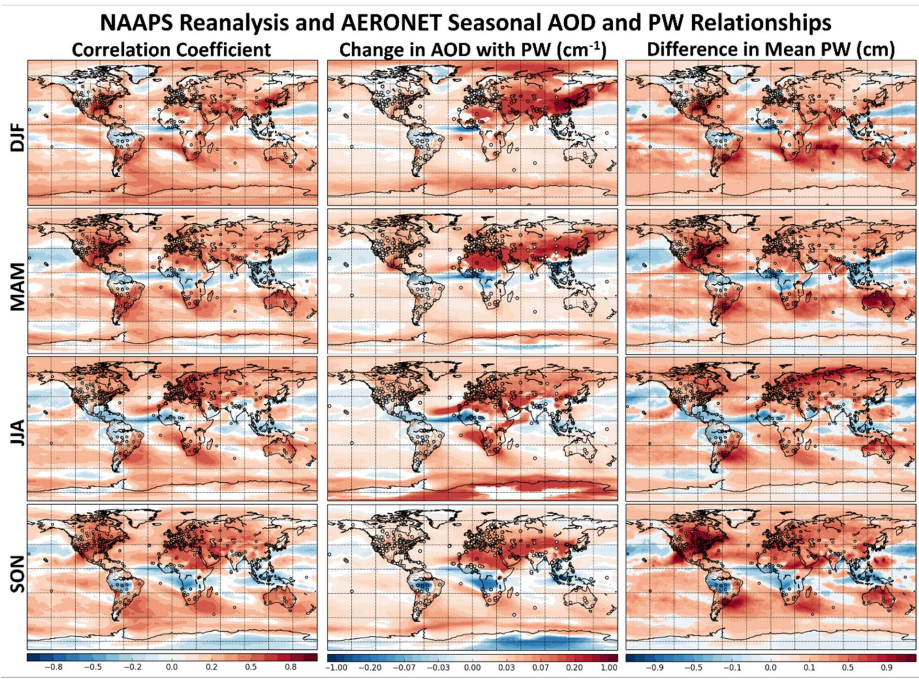


858

859 Figure 6. NAAPS-RA PW percentiles by season (DJF, MAM, JJA, SON). The 25th and 75th percentiles are shown along
 860 with the interquartile range (IQR). The 90th percentile is used to show high PW values at a given location.

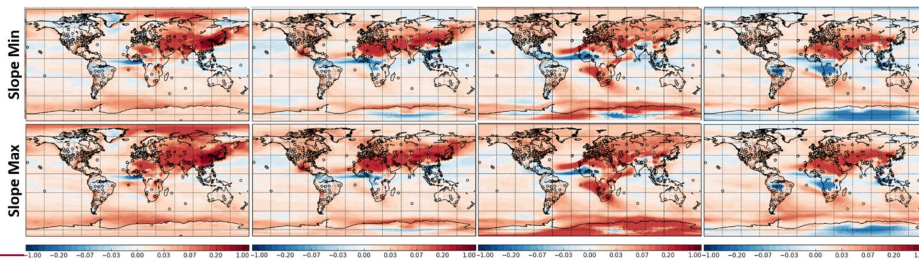


861

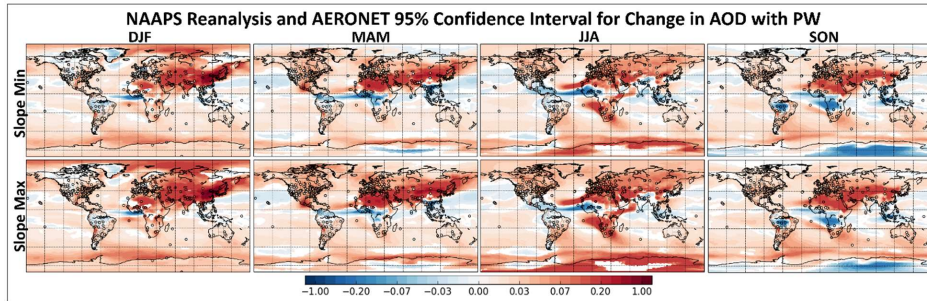


862

863 Figure 7. Seasonal AOD and PW relationships based on AERONET data (circles) and the NAAPS-RA (global map) shown
 864 as: **1a)** correlation coefficients between daily-averaged AOD and PW (non-zero values are statistically significant at the
 865 95% level) **b2)** Theil-Sen regression slopes (change in AOD with PW) between daily-averaged AOD and PW in units of cm⁻¹
 866 at locations where the correlation is statistically significant and **e3)** the statistically significant difference in mean PW (cm)
 867 between the PW distribution associated with high AOD events (> 1 standard deviation above mean) and the PW distribution
 868 for all AOD values. Red regions indicate a positive relationship between AOD and PW (higher moisture conditions for
 869 higher AOD events) and blue regions indicate a negative relationship (drier conditions for higher AOD events).



870



871

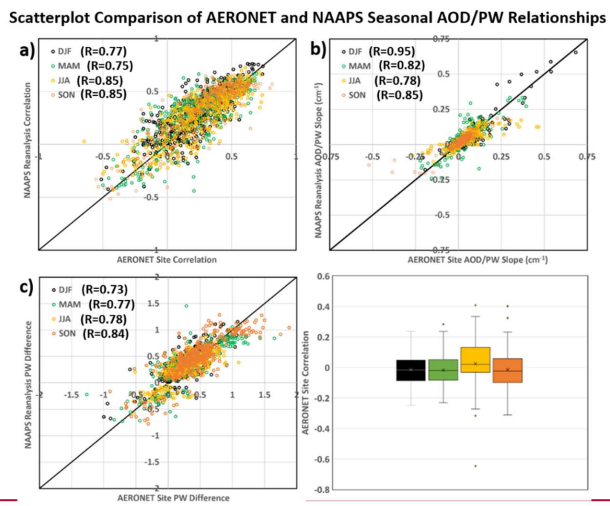
872 Figure 8. The 95% confidence interval in the Theil-Sen change in AOD with PW (cm^{-1}) for DJF, MAM, JJA, and SON. The
 873 confidence intervals are shown for both the NAAPS-RA and AERONET.

Formatted: Superscript

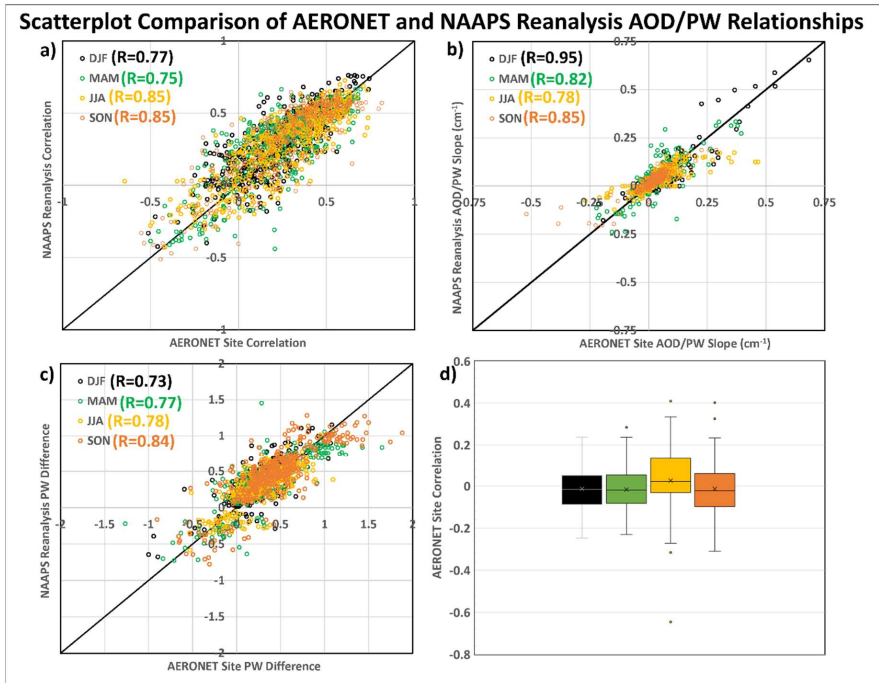
874

875

876



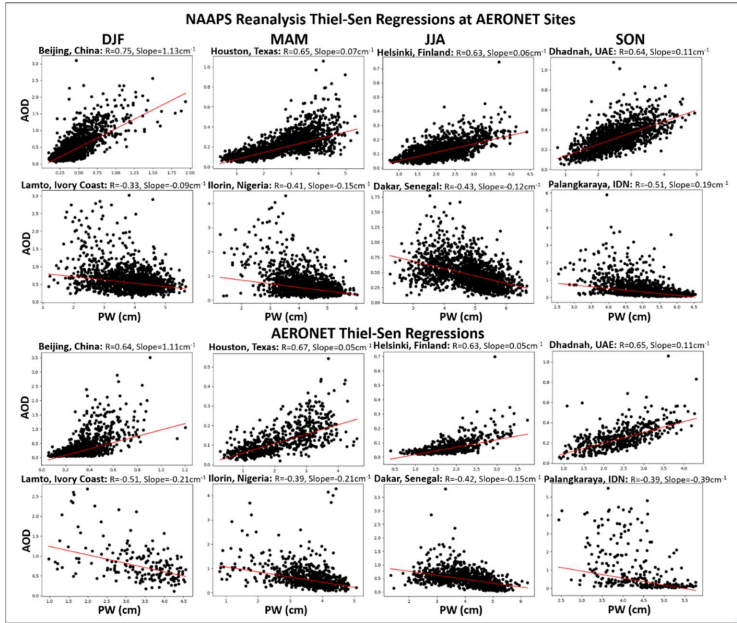
877

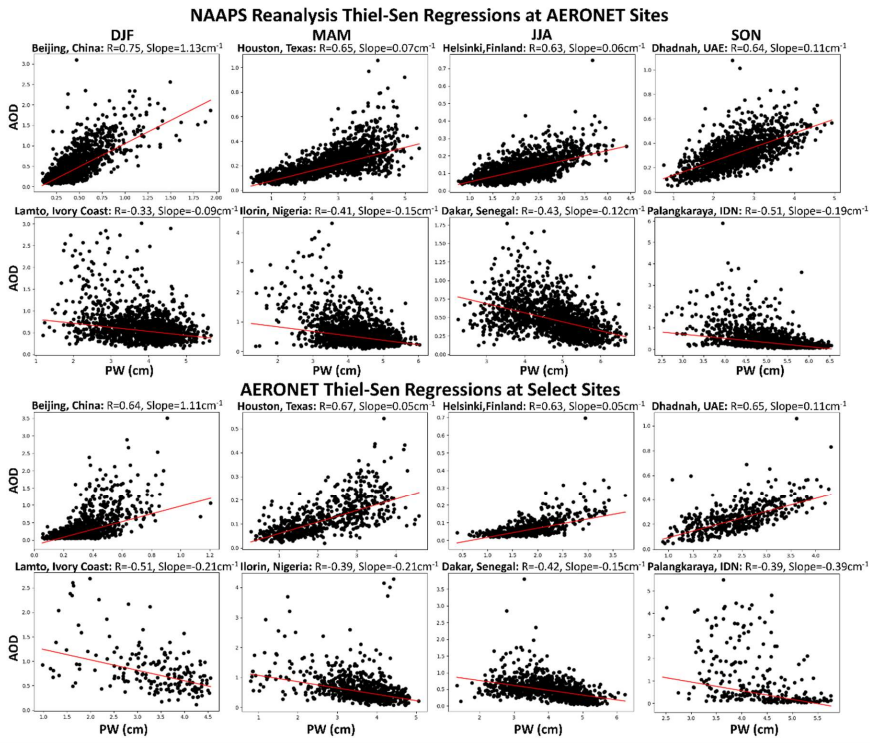


878

879 Figure 9. Scatterplot comparisons of the NAAPS-RA and AERONET: a) AOD and PW correlations at AERONET sites b)
 880 the change in AOD with PW (cm^{-1}) at AERONET sites and c) the statistically significant difference in mean PW associated
 881 with high AOD events compared to the full PW distribution at AERONET sites. The comparisons are shown by season
 882 (DJF, MAM, SON, JJA) and correlations between the datasets are included. Additionally, the distribution of AERONET
 883 site correlations for which sign differences were found between NAAPS and AERONET calculated AOD/PW relationships
 884 are shown seasonally in d).

885

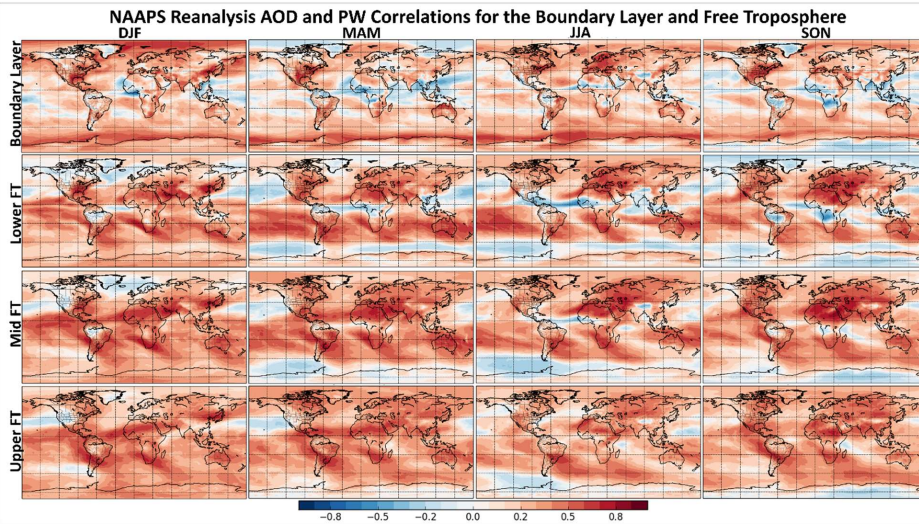
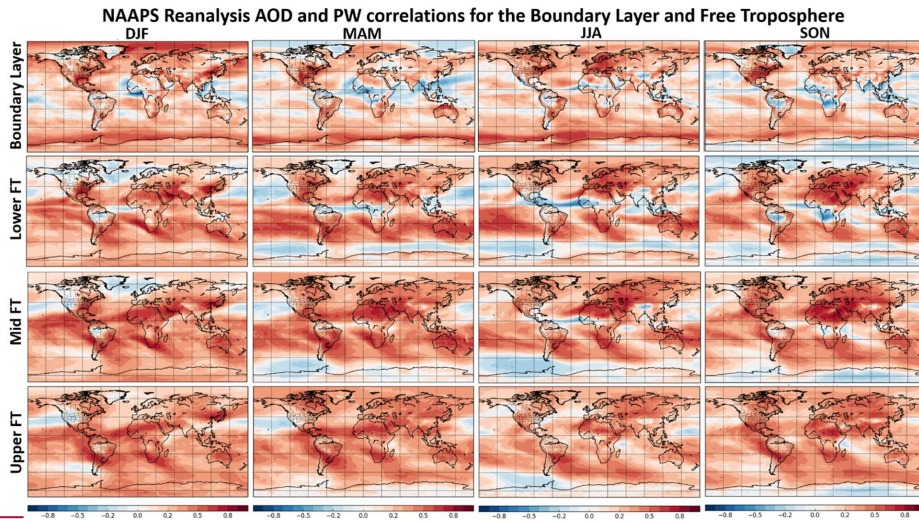




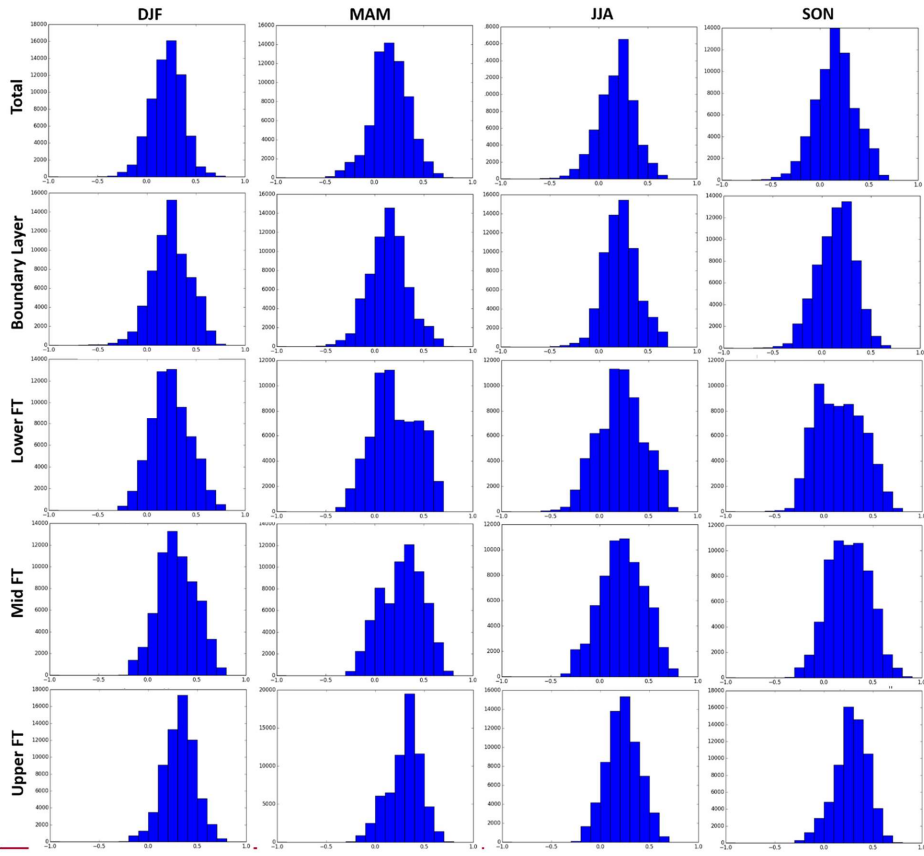
887
 888 Figure 10. Seasonal examples of NAAPS-RA and AERONET Thiel-Sen regression calculations for positive correlation
 889 locations (Beijing, Houston, Helsinki, Dhadnah) and a negative correlation locations (Lamto, Ilorin, Dakar, Palangkaraya).
 890 The black dots are the AOD and PW pairs from the NAAPS-RA or AERONET and the red line is the Thiel-Sen fitting,
 891 which is the median of the slopes for the range of data pairings. The location name, correlation coefficient (R), and the
 892 Thiel-Sen slope (Slope) are included with each plot.

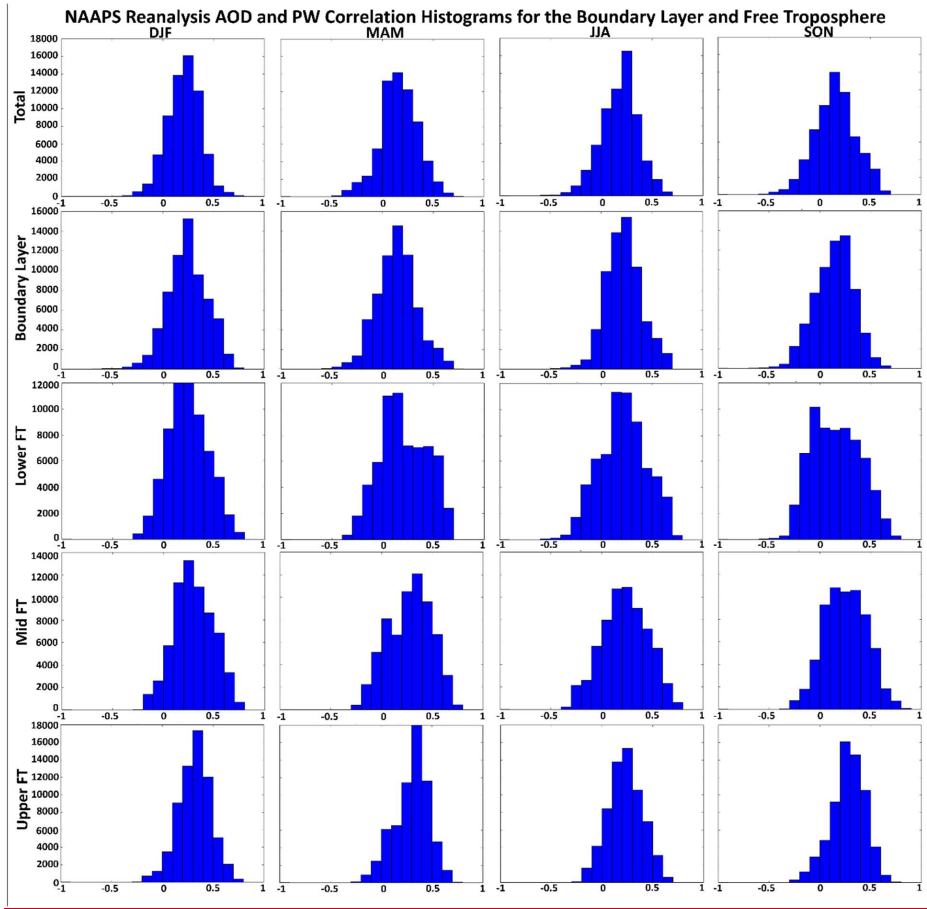
893

894



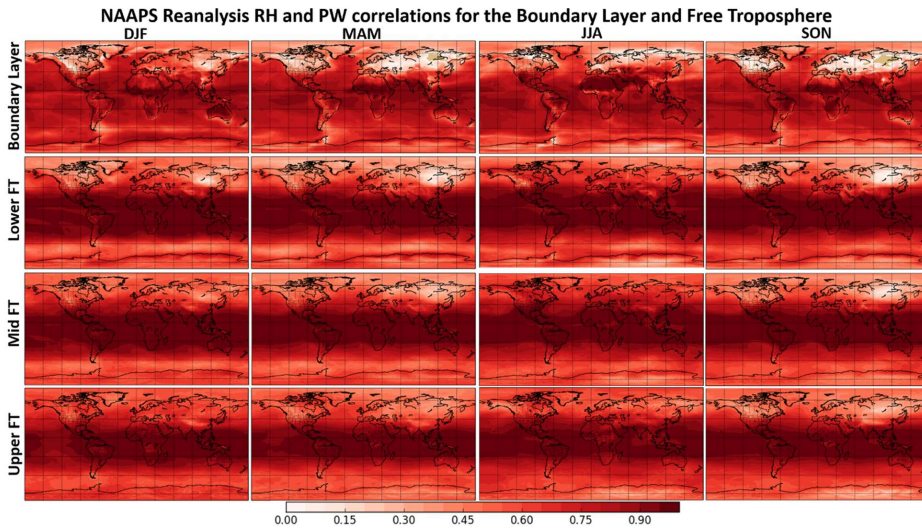
897 Figure 11. NAAPS-RA seasonal correlations (DJF, MAM, JJA, SON) between vertically-integrated total aerosol extinction
 898 and specific humidity in the boundary layer, lower free troposphere, mid free troposphere and upper free troposphere. Red
 899 values indicate a positive correlation and blue values indicate a negative correlation.





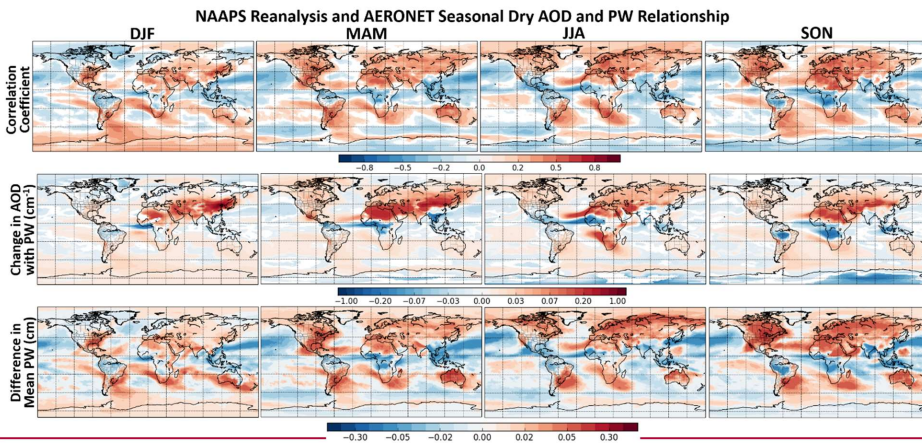
901

902 Figure 12. AOD and PW correlation histograms by season for the full integrated column (Total) and vertical components
 903 of the atmosphere (Boundary Layer, Lower/Mid/Upper Free Troposphere).

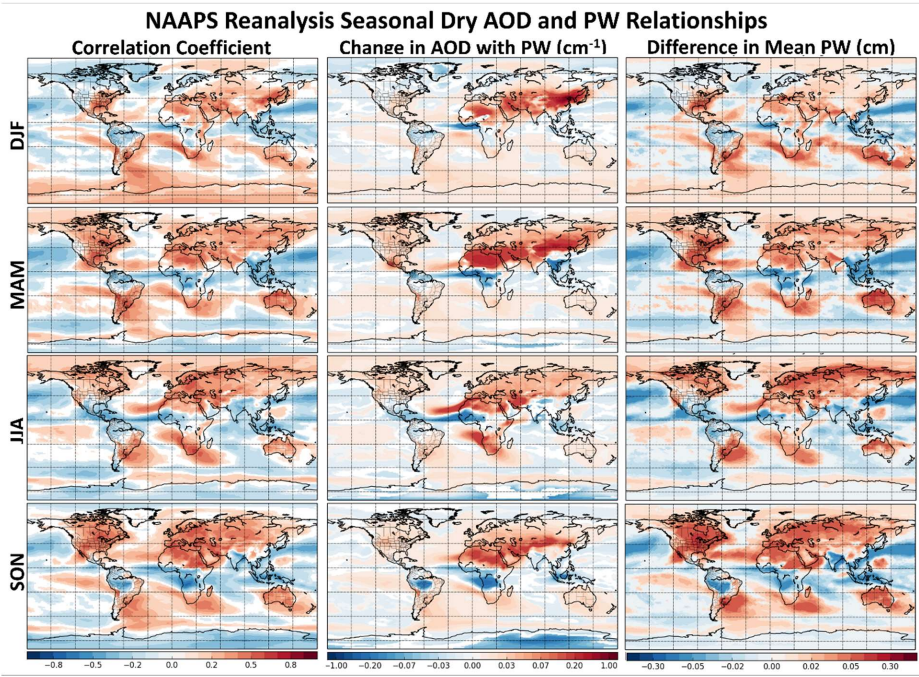


904
 905 Figure 13. NAAPS-RA seasonal correlations (DJF, MAM, JJA, SON) between vertically-integrated relative humidity
 906 (integrated specific humidity/integrated saturation specific humidity) and specific humidity in the boundary layer, lower
 907 free troposphere, mid free troposphere and upper free troposphere.

908

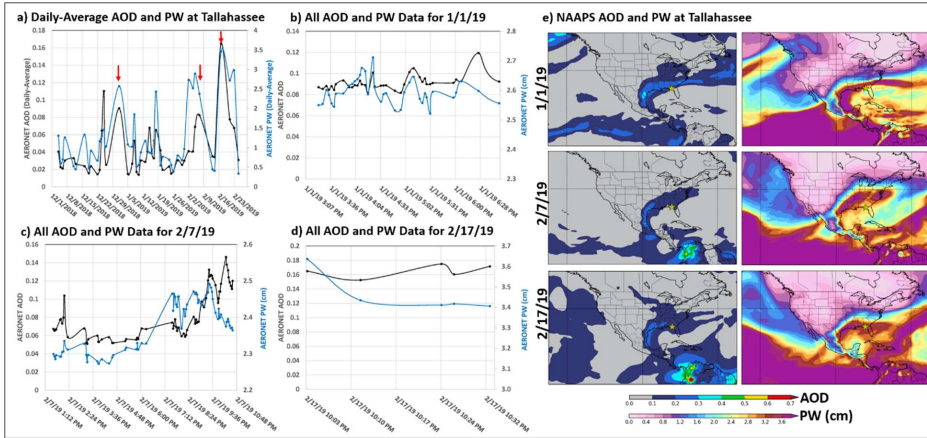


909

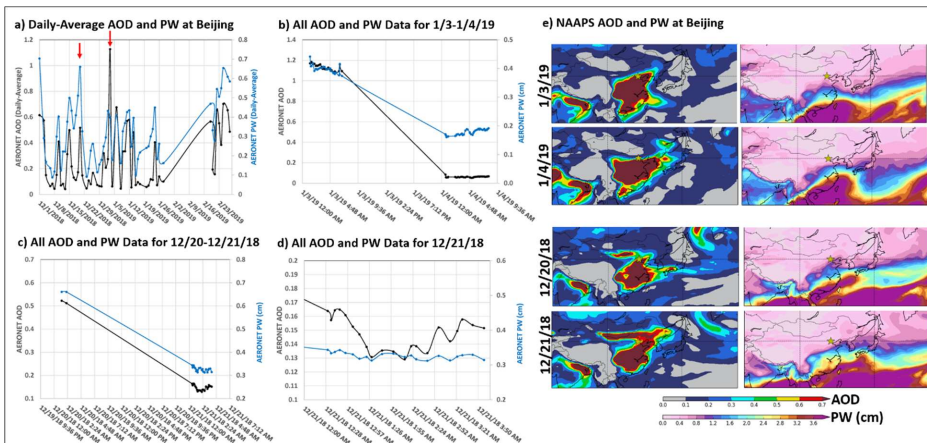


910

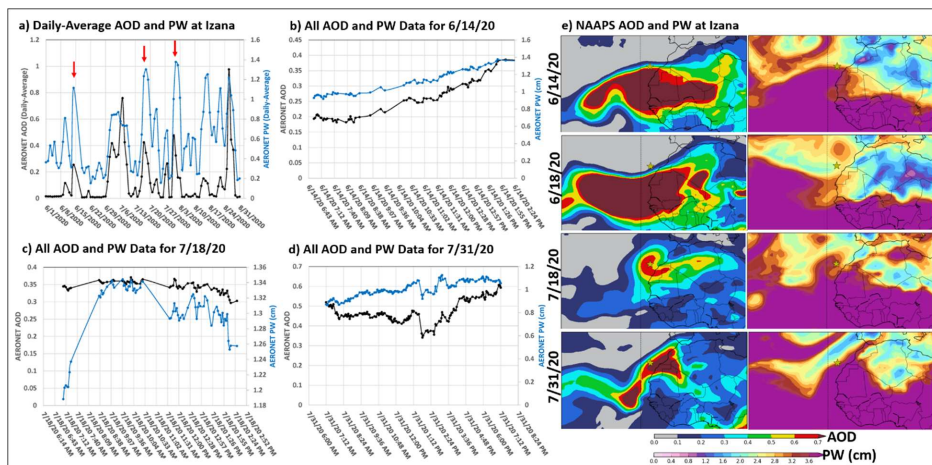
911 Figure 14. Seasonal dry AOD and PW relationships based on the NAAPS-RA shown as: **1)** correlation coefficients between
 912 daily-averaged dry AOD and PW (non-zero values are statistically significant at the 95% level) **2)** Theil-Sen regression
 913 slopes (change in AOD with PW) between daily-averaged dry AOD and PW in units of cm⁻¹ at locations where the
 914 correlation is statistically significant and **3)** the statistically significant difference in mean PW (cm) between the PW
 915 distribution associated with high dry AOD events (> 1 standard deviation above mean) and the PW distribution for all AOD
 916 values. Red regions indicate a positive relationship between dry AOD and PW and blue regions indicate a negative
 917 relationship.



918
 919 Figure 15. AOD and PW timeseries at the Tallahassee, Florida site in which strong positive correlations are observed during the DJF season. The daily-average AOD and PW timeseries are shown for the 2018-2019 DJF season with red arrows
 920 indicating select events for which joint peaks in AOD and PW are observed (a). Timeseries of AERONET data (non-
 921 averaged, all data) for dates identified with red arrows are shown in timeseries b-d. Additionally, NAAPS-RA AOD and
 922 PW (cm) fields are shown for the same dates with the AERONET site marked with a yellow star (e).
 923

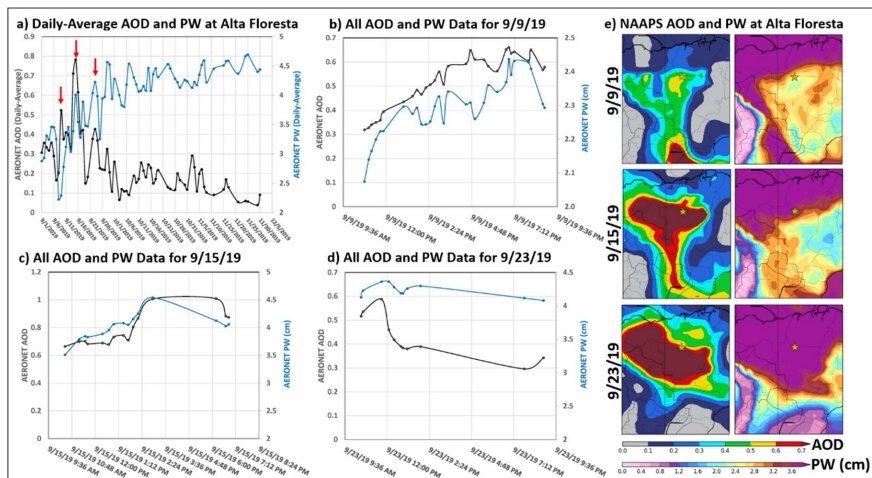


924
 925 Figure 16. AOD and PW timeseries at the Beijing, China site in which strong positive correlations are observed during the
 926 DJF season. The daily-average AOD and PW timeseries are shown for the 2018-2019 DJF season with red arrows indicating
 927 select events for which joint peaks in AOD and PW are observed (a). Timeseries of AERONET data (non-averaged, all
 928 data) for dates identified with red arrows are shown in timeseries b-d. Additionally, NAAPS-RA AOD and PW (cm)
 929 are shown for the same dates with the AERONET site marked with a yellow star (e), including the air mass movement for
 930 1/3-1/4/19 and 12/20-12/21/18.



931
 932 Figure 17. AOD and PW timeseries at the Izana, Canary Islands site in which strong positive correlations are observed
 933 during the JJA season. The daily-average AOD and PW timeseries are shown for the 2020 JJA season with red arrows
 934 indicating select events for which joint peaks in AOD and PW are observed (a). Timeseries of AERONET data (non-
 935 averaged, all data) for dates identified with red arrows are shown in timeseries b-d. Additionally, NAAPS-RA AOD and PW
 936 (cm) fields are shown for the same dates with the AERONET site marked with a yellow star (e). The fields for 6/18/20
 937 are also included which show the joint dip in AOD and PW in the (a) timeseries after the 6/14 event.

938



940 Figure 18. AOD and PW timeseries at the Alta Floresta site in Brazil in which negative AOD and PW correlations were
 941 identified in the seasonal analysis. The daily-average AOD and PW timeseries are shown for the 2019 SON season with red
 942 arrows indicating select events for further evaluation (a). AERONET AOD and PW timeseries (non-averaged, all data) for
 943 the selected events are shown in timeseries b-d. Additionally, NAAPS-RA AOD and PW (cm) fields are shown for the same
 944 dates with the AERONET site marked with a yellow star (e).

945 **Table 1. AOD and PW relationship evaluation results for DJF at select AERONET sites that exhibited the strongest**
 946 **AERONET correlations, positive and negative. The site name and latitude/longitude information are shown as well as the**
 947 **correlation (R), change in AOD with PW (Slope), and the statistically significant difference in mean PW for high AOD**
 948 **events (PW Diff) for both AERONET and the NAAPS-RA.**

AERONET Site	Lat	Lon	AERONET			NAAPS Reanalysis		
			R	Slope (cm ⁻¹)	PW Diff (cm)	R	Slope (cm ⁻¹)	PW Diff (cm)
Stennis	30.37	-89.62	0.743	0.044	1.082	0.739	0.042	1.156
Tallahassee	30.45	-84.30	0.739	0.024	1.068	0.664	0.037	0.901
Beijing-CAMS	39.93	116.32	0.707	1.016	0.225	0.755	1.132	0.347
XiangHe	39.75	116.96	0.673	1.349	0.196	0.755	1.132	0.347
SEARCH-Centreville	32.90	-87.25	0.665	0.028	0.931	0.706	0.045	1.000
Univ_of_Houston	29.72	-95.34	0.661	0.039	0.734	0.762	0.058	1.109
SEARCH-OLF	30.55	-87.38	0.659	0.025	0.820	0.720	0.039	1.069
Beijing	39.98	116.38	0.638	1.108	0.211	0.755	1.132	0.347
UAHuntsville	34.73	-86.64	0.633	0.029	0.930	0.684	0.049	0.866
UH_Coastal_Center	29.39	-95.04	0.624	0.039	0.862	0.762	0.058	1.109
Dhadnah	25.51	56.32	0.610	0.120	0.535	0.548	0.110	0.653
Ilorin	8.48	4.67	-0.261	-0.100	-0.513	-0.159	-0.063	-0.356
Pontianak	0.08	109.19	-0.345	-0.054	-0.476	-0.255	-0.029	-0.278
Kofofidua_ANUC	6.11	-0.30	-0.459	-0.194	-0.894	-0.424	-0.178	-0.676
Jambi	-1.63	103.64	-0.473	-0.110	-0.942	-0.217	-0.039	-0.392
LAMTO-STATION	6.22	-5.03	-0.513	-0.214	-0.999	-0.331	-0.093	-0.644

949

950 **Table 2. AOD and PW relationship evaluation results for MAM at select AERONET sites that exhibited the strongest**
 951 **AERONET correlations, positive and negative. The site name and latitude/longitude information are shown as well as the**
 952 **correlation (R), change in AOD with PW (Slope), and the statistically significant difference in mean PW for high AOD**
 953 **events (PW Diff) for both AERONET and the NAAPS-RA.**

AERONET Site	Lat	Lon	AERONET			NAAPS Reanalysis		
			R	Slope (cm ⁻¹)	PW Diff (cm)	R	Slope (cm ⁻¹)	PW Diff (cm)
UH_Coastal_Center	29.39	-95.04	0.694	0.041	1.099	0.665	0.068	1.058
UMBC	39.25	-76.71	0.680	0.042	1.219	0.602	0.053	0.870
Stennis	30.37	-89.62	0.680	0.046	0.967	0.630	0.048	0.978
NEON_OSBS	29.69	-81.99	0.679	0.032	1.241	0.511	0.038	0.737
NEON_TALL	32.95	-87.39	0.677	0.032	0.915	0.604	0.047	0.815
Univ_of_Houston	29.72	-95.34	0.666	0.048	1.000	0.665	0.068	1.058
UAHuntsville	34.73	-86.64	0.664	0.049	0.992	0.611	0.050	0.766
CCNY	40.82	-73.95	0.663	0.056	1.132	0.614	0.056	0.889
CASLEO	-31.80	-69.30	0.652	0.020	0.342	0.432	0.044	0.218
NEON_ORNL	35.96	-84.28	0.649	0.033	1.007	0.586	0.051	0.698
Nainital	29.36	79.46	0.629	0.256	0.422	0.388	0.112	0.457
Midway_Island	28.21	-177.38	-0.326	-0.033	-0.370	-0.323	-0.026	-0.490
Mandalay_MTU	21.97	96.19	-0.338	-0.049	-0.439	-0.384	-0.080	-0.717
LAMTO-STATION	6.22	-5.03	-0.353	-0.177	-0.429	-0.321	-0.132	-0.350
Vientiane	17.99	102.57	-0.355	-0.130	-0.451	-0.377	-0.144	-0.408
Chiang_Mai_Met_St	18.77	98.97	-0.372	-0.109	-0.586	-0.391	-0.126	-0.554
Jambi	-1.63	103.64	-0.392	-0.034	-1.265	-0.206	-0.020	-0.220
Ilorin	8.48	4.67	-0.392	-0.210	-0.710	-0.412	-0.151	-0.726
NGHIA_DO	21.05	105.80	-0.455	-0.216	-0.632	-0.318	-0.166	-0.349
Djougou	9.76	1.60	-0.500	-0.222	-0.836	-0.385	-0.114	-0.700

954

955

956

957 Table 3. AOD and PW relationship evaluation results for JJA at select AERONET sites that exhibited the strongest
 958 AERONET correlations, positive and negative. The site name and latitude/longitude information are shown as well as the
 959 correlation (R), change in AOD with PW (Slope), and the statistically significant difference in mean PW for high AOD
 960 events (PW Diff) for both AERONET and the NAAPS-RA. PW difference values of 0 in the NAAPS-RA indicate the change
 961 was not statistically significant.

AERONET Site	Lat	Lon	AERONET			NAAPS Reanalysis		
			R	Slope (cm ⁻¹)	PW Diff (cm)	R	Slope (cm ⁻¹)	PW Diff (cm)
Huambo	-12.87	15.70	0.737	0.365	0.447	0.467	0.174	0.350
DRAGON_OLNES	39.15	-77.07	0.731	0.088	0.894	0.399	0.048	0.386
Pretoria_CSIR-DPSS	-25.76	28.28	0.731	0.140	0.438	0.660	0.120	0.446
DRAGON_CLLGP	38.99	-76.91	0.719	0.085	1.097	0.348	0.039	0.387
Durban_UKZN	-29.82	30.94	0.711	0.111	0.670	0.687	0.131	0.567
Raciborz	50.08	18.19	0.672	0.065	0.749	0.614	0.085	0.578
Izana	28.31	-16.50	0.662	0.240	0.345	0.477	0.152	0.495
Helsinki	60.20	24.96	0.633	0.052	0.790	0.631	0.060	0.698
IMS-METU-ERDEML	36.57	34.26	0.632	0.099	0.543	0.559	0.073	0.484
CLUJ_UBB	46.77	23.55	0.632	0.091	0.529	0.602	0.100	0.438
Pokhara	28.19	83.98	-0.349	-0.111	-0.452	0.029	0.026	0.000
Bidi_Bahn	14.06	-2.45	-0.360	-0.175	-0.244	-0.251	-0.060	-0.305
Ouagadougou	12.42	-1.49	-0.385	-0.180	-0.292	-0.205	-0.059	-0.211
Lumbini	27.49	83.28	-0.388	-0.157	-0.434	-0.098	-0.013	-0.171
Dakar	14.39	-16.96	-0.418	-0.146	-0.528	-0.428	-0.122	-0.584
Agoufou	15.35	-1.48	-0.491	-0.209	-0.533	-0.258	-0.060	-0.346
IER_Cinzana	13.28	-5.93	-0.501	-0.269	-0.424	-0.279	-0.077	-0.259
Jomsom	28.78	83.71	-0.646	-0.064	-0.581	0.029	0.026	0.000

962

963 Table 4. AOD and PW relationship evaluation results for SON at select AERONET sites that exhibited the strongest
 964 AERONET correlations, positive and negative. The site name and latitude/longitude information are shown as well as the
 965 correlation (R), change in AOD with PW (Slope), and the statistically significant difference in mean PW for high AOD
 966 events (PW Diff) for both AERONET and the NAAPS-RA. PW difference values of 0 in the NAAPS-RA indicate the change
 967 was not statistically significant.

AERONET Site	Lat	Lon	AERONET			NAAPS Reanalysis		
			R	Slope (cm ⁻¹)	PW Diff (cm)	R	Slope (cm ⁻¹)	PW Diff (cm)
USDA	39.03	-76.88	0.815	0.088	1.883	0.570	0.036	1.043
SEARCH-Centreville	32.90	-87.25	0.796	0.026	1.748	0.531	0.032	0.917
St_Louis_University	38.64	-90.23	0.724	0.032	1.369	0.574	0.037	1.188
Martova	49.94	36.95	0.706	0.070	0.590	0.531	0.064	0.633
UMBC	39.25	-76.71	0.699	0.035	1.473	0.570	0.036	1.043
Poprad-Ganovce	49.04	20.32	0.689	0.053	0.651	0.568	0.071	0.525
NEON_TALL	32.95	-87.39	0.679	0.025	1.184	0.531	0.032	0.917
GISS	40.80	-73.96	0.673	0.062	1.369	0.556	0.033	0.950
Harvard_Forest	42.53	-72.19	0.666	0.035	1.051	0.576	0.036	1.020
Mingo	36.97	-90.14	0.655	0.040	1.500	0.594	0.038	1.186
Dhadnah	25.51	56.32	0.651	0.106	0.757	0.643	0.115	0.706
Midway_Island	28.21	-177.38	-0.344	-0.013	-0.431	-0.172	-0.007	-0.339
Alta_Floresta	-9.87	-56.10	-0.382	-0.148	-0.573	-0.470	-0.197	-0.634
Koforidua_ANUC	6.11	-0.30	-0.384	-0.161	-0.173	-0.252	-0.046	-0.330
Rio_Branco	-9.96	-67.87	-0.426	-0.121	-0.496	-0.430	-0.145	-0.643
Abracos_Hill	-10.76	-62.36	-0.430	-0.226	-0.351	-0.401	-0.205	-0.373
Ilorin	8.48	4.67	-0.431	-0.091	-0.653	-0.227	-0.033	-0.476
Palangkaraya	-2.23	113.95	-0.443	-0.385	-0.549	-0.512	-0.195	-0.886
Ji_Parana_SE	-10.93	-61.85	-0.483	-0.197	-0.659	-0.412	-0.203	-0.393
Pontianak	0.08	109.19	-0.536	-0.521	-0.644	-0.400	-0.145	-0.454
Kuching	1.49	110.35	-0.552	-0.373	-0.528	-0.329	-0.111	-0.360

968

969 **References**

- 970 American Meteorological Society, 2020: Aerosol. Glossary of
971 Meteorology, <http://glossary.ametsoc.org/wiki/climatology>. Last accessed Jan 2021.
- 972 Adebisi, A. A., Zuidema, P., and Abel, S. J.: The Convolution of Dynamics and Moisture with the Presence of
973 Shortwave Absorbing Aerosols over the Southeast Atlantic, *Journal of Climate*, 28, 1997–2024,
974 <https://doi.org/10.1175/JCLI-D-14-00352.1>, 2015.
- 975 Arola, A., Eck, T. F., Kokkola, H., Pitkänen, M. R. A., and Romakkaniemi, S.: Assessment of cloud-related fine-
976 mode AOD enhancements based on AERONET SDA product, *Atmos. Chem. Phys.*, 17, 5991–6001,
977 <https://doi.org/10.5194/acp-17-5991-2017>, 2017.
- 978 Barreto, Á., Cuevas, E., García, R. D., Carrillo, J., Prospero, J. M., Ilić, L., Basart, S., Berjón, A. J., Marrero, C. L.,
979 Hernández, Y., Bustos, J. J., Ničković, S., and Yela, M.: Long-term characterization of the vertical structure of the
980 Saharan Air Layer over the Canary Islands using lidar and radiosonde profiles: implications for radiative and cloud
981 processes over the subtropical Atlantic Ocean, *Atmos. Chem. Phys.*, 22, 739–763, [https://doi.org/10.5194/acp-22-](https://doi.org/10.5194/acp-22-739-2022)
982 [739-2022](https://doi.org/10.5194/acp-22-739-2022), 2022.
- 983 Benedetti, A., Morcrette, J.-J., Boucher, O., Dethof, A., Engelen, R. J., Fisher, M., Flentje, H., Huneeus, N., Jones,
984 L., Kaiser, J. W., Kinne, S., Mangold, A., Razinger, M., Simmons, A. J., and Suttie, M.: Aerosol analysis and recast
985 in the European centre for Medium-Range Weather Forecasts Integrated Forecast
986 System: 2. Data assimilation, *J. Geophys. Res.*, 114, D13205, doi:10.1029/2008JD011115, 2009.
- 987 Charlson, R.J., S.E. Schwartz, J.M. Hales, R.D. Cess, J.A. Coakley, Jr., J.E. Hansen, and D.J. Hoffman: Climate
988 forcing by anthropogenic aerosols. *Science*, 255, 423-430, doi:10.1126/science.255.5043.423, 1992.
- 989 Daley, R. and Barker, E.: NAVDAS: Formulation and diagnostics, *Mon. Weather Rev.*, 129, 869–883,
990 [https://doi.org/10.1175/1520-0493\(2001\)129](https://doi.org/10.1175/1520-0493(2001)129), 2001.
- 991 Deaconu, L. T., Ferlay, N., Waquet, F., Peers, F., Thieuleux, F., and Goloub, P.: Satellite inference of water vapour
992 and above-cloud aerosol combined effect on radiative budget and cloud-top processes in the southeastern Atlantic
993 Ocean, *Atmos. Chem. Phys.*, 19, 11613–11634, <https://doi.org/10.5194/acp-19-11613-2019>, 2019.
- 994 DeSouza-Machado, S. G., Strow, L. L., Hannon, S. E., and Motteler, H. E.: Infrared dust spectral signatures from
995 AIRS, *Geophys. Res. Lett.*, 33, L03801, doi:10.1029/2005GL024364, 2006.
- 996 De Tomasi, F., and Perrone, M. R.: Lidar measurements of tropospheric water vapor and aerosol profiles over
997 southeastern Italy, *J. Geophys. Res.*, 108, 4286, doi:10.1029/2002JD002781, 2003.
- 998 Eck, T. F., and Holben, B. N.: AVHRR split window temperature differences and total precipitable water over land
999 surfaces, *International Journal of Remote Sensing*, 15:3, 567-582, doi: 10.1080/01431169408954097, 1994.
- 1000 Eck, T. F., Holben B. N., Reid, J. S., Dubovik, O., Smirnov, A., O'Neill, N. T., Slutsker, I., and Kinne, S.:
1001 Wavelength dependence of the optical depth of biomass burning, urban, and desert
1002 dust aerosols, *J. Geophys. Res.*, 104, 31333–31349, DOI: 10.1029/1999JD900923, 1999.
- 1003 Eck, T.F., Holben, B.N., Reid, J.S., Giles, D.M., Rivas, M.A., Singh, R.P., Tripathi, S.N., Bruegge, C.J., Platnick,
1004 S., Arnold, G.T., Krotkov, N.A., Carn, S.A., Sinyuk, A., Dubovik, O., Arola, A., Schafer, J.S., Artaxo, P., Smirnov,
1005 A., Chen, H., Goloub, P.: Fog- and cloud-induced aerosol modification observed by the Aerosol Robotic Network
1006 (AERONET), *J. Geophys. Res.*, 117, D07206,doi:10.1029/2011JD016839, 2012.
- 1007 Eck, T. F., Holben, B. N., Reid, J. S., Arola, A., Ferrare, R. A., Hostetler, C. A., Crumeyrolle, S. N., Berkoff, T. A.,
1008 Welton, E. J., Lolli, S., Lyapustin, A., Wang, Y., Schafer, J. S., Giles, D. M., Anderson, B. E., Thornhill, K. L.,
1009 Minnis, P., Pickering, K. E., Loughner, C. P., Smirnov, A., and Sinyuk, A.: Observations of rapid aerosol optical
1010 depth enhancements in the vicinity of polluted cumulus clouds, *Atmos. Chem. Phys.*, 14, 11633–11656,
1011 <https://doi.org/10.5194/acp-14-11633-2014>, 2014.
- 1012 Eck, T. F., Holben, B. N., Reid, J. S., Xian, P., Giles, D. M., Sinyuk, A., Smirnov, A., Schafer, J.S., Slutsker, I., Kim,
1013 J., Koo, J.-H., Choi, M., Kim, K.C., Sano, I., Arola, A., Sayer, A.M., Levy, R.C., Munchak, L.A., O'Neill, N.T.,
1014 Lyapustin, A., Hsu, N.C., Randles, C.A., Da Silva, A.M., Buchard, V., Govindaraju, R.C., Hyer, E., Crawford, J.H.,
1015 Wang, P., Xia, X.: Observations of the interaction and transport of fine mode aerosols with cloud and/or fog in

1016 Northeast Asia from Aerosol Robotic Network and satellite remote sensing. *Journal of Geophysical Research: Atmospheres*, 123, 5560–5587. <https://doi.org/10.1029/2018JD028313>, 2018.

1017

1018 Eck, T.F., Holben, B.N., Giles, D.M., Slutsker, I., Sinyuk, A., Schafer, J.S., Smirnov, A., Sorokin, M., Reid, J.S.,
1019 Sayer, A.M., Hsu, N.C., Shi, Y.R., Levy, R.C., Lyapustin, A., Rahman, M.A., Liew, S.-C., Cortijo, S.V.S., Li, R.,
1020 Kalbermatter, D., Keong, K.L., Yuggotomo, M.E., Aditya, F., Mohamad, M., Mahmud, M., Chong, T.K., Lim, H.-
1021 S., Choon, Y.E., Deranadyan, G., Kusumaningtyas, S.D.A., Aldrian, E.: AERONET Remotely Sensed
1022 Measurements and Retrievals of Biomass Burning Aerosol Optical Properties During the 2015 Indonesian Burning
1023 Season, *J. Geophys. Res.*, 124, 4722–4740. <https://doi.org/10.1029/2018JD030182>, 2019.

1024 Francis, D., Fonseca, R., Nelli, N., Cuesta, J., Weston, M., Evan, A., and Temimi, M: The atmospheric drivers of the
1025 major Saharan dust storm in June 2020, *Geophys. Res. Lett.*, 47, e2020GL090102.
1026 <https://doi.org/10.1029/2020GL090102>, 2020.

1027 Frouin, R.J., Franz, B.A., Ibrahim, A., Knobelspiess, K., Ahmad, Z., Cairns, B., Chowdhary, J., Dierssen, H.M.,
1028 Tan, J., Dubovik, O., Huang, X., Davis, A.B., Kalashnikova, O., Thompson, D.R., Remer, L.A., Boss, E.,
1029 Coddington, O., Deschamps, P.-Y., Gao, B.-C., Gross, L., Hasekamp, O., Omar, A., Pelletier, B., Ramon, D.,
1030 Steinmetz, F., and Zhai, P.-W.: Atmospheric correction of satellite ocean-color imagery during the PACE Era. *Front.*
1031 *Earth Sci.*, 7, 145, doi:10.3389/feart.2019.00145, 2019.

1032 Gao, M., Carmichael, G. R., Saide, P. E., Lu, Z., Yu, M., Streets, D. G., and Wang, Z.: Response of winter fine
1033 particulate matter concentrations to emission and meteorology changes in North China, *Atmos. Chem. Phys.*, 16,
1034 11837–11851, <https://doi.org/10.5194/acp-16-11837-2016>, 2016.

1035 Giles, D. M., Sinyuk, A., Sorokin, M. G., Schafer, J. S., Smirnov, A., Slutsker, I., Eck, T. F., Holben, B. N., Lewis,
1036 J. R., Campbell, J. R., Welton, E. J., Korkin, S. V., and Lyapustin, A. I.: Advancements in the Aerosol Robotic
1037 Network (AERONET) Version 3 database – automated near-real-time quality control algorithm with improved
1038 cloud screening for Sun photometer aerosol optical depth (AOD) measurements, *Atmos. Meas. Tech.*, 12, 169–209,
1039 <https://doi.org/10.5194/amt-12-169-2019>, 2019.

1040 Gobbi, G.P., Barnaba, F., Di Liberto, L., Bolignano, A., Lucarelli, F., Nava, S., Perrino, C., Pietrodangelo, A.,
1041 Basart, S., Costabile, F., Dionisi, D., Rizza, U., Canepari, S., Sozzi, R., Morelli, M., Manigrasso, M., Drewnick, F.,
1042 Struckmeier, C., Poenitz, K., Wille, H.: An inclusive view of Saharan dust advections to Italy and the Central
1043 Mediterranean, *Atmospheric Environment*, Volume 201, 2019, Pages 242-256, ISSN 1352-2310,
1044 <https://doi.org/10.1016/j.atmosenv.2019.01.002>, 2019.

1045 Granados-Muñoz, M. J., Sicard, M., Román, R., Benavent-Oltra, J. A., Barragán, R., Brogniez, G., Denjean, C.,
1046 Mallet, M., Formenti, P., Torres, B., and Alados-Arboledas, L.: Impact of mineral dust on shortwave and longwave
1047 radiation: evaluation of different vertically resolved parameterizations in 1-D radiative transfer computations,
1048 *Atmos. Chem. Phys.*, 19, 523–542, <https://doi.org/10.5194/acp-19-523-2019>, 2019.

1049 Gutleben, M., Groß, S., Wirth, M., Emde, C., & Mayer, B.: Impacts of water vapor on Saharan air layer radiative
1050 heating. *Geophysical Research Letters*, 46, 14854–14862, <https://doi.org/10.1029/2019GL085344>, 2019.

1051 Haywood, J. M., Bellouin, N., Jones, A., Boucher, O., Wild, M., and Shine, K. P.: The roles of aerosol, water vapor
1052 and cloud in future global dimming/brightening, *J. Geophys. Res.*, 116, D20203, doi:10.1029/2011JD016000, 2011.

1053 Hänel, G.: The properties of atmospheric aerosol particles as functions of the relative humidity at thermo- dynamic
1054 equilibrium with the surrounding moist air. *Adv. Geophys.* 19, 73-18, [https://doi.org/10.1016/S0065-](https://doi.org/10.1016/S0065-2687(08)60142-9)
1055 [2687\(08\)60142-9](https://doi.org/10.1016/S0065-2687(08)60142-9), 1976.

1056 He Q., Ma, J., Zheng, X., Wang, Y., Wang Y., Mu, H., Cheng, T., He, R., Huang, G., Liu, D.: Formation and
1057 dissipation dynamics of the Asian tropopause aerosol layer, *Environ. Res. Lett.*, 16, 014015,
1058 <https://doi.org/10.1088/1748-9326/abcd5d>, 2021.

1059 Heo, J.-H.; Ryu, G.-H.; Jang, J.-D. Optimal Interpolation of Precipitable Water Using Low Earth Orbit and
1060 Numerical Weather Prediction Data. *Remote Sens.* 2018, 10, 436.

1061 Hogan, T. F., Liu, M., Ridout, J. S., Peng, M. S., Whitcomb, T. R., Ruston, B. C., Reynolds, C. A., Eckermann S.
1062 D., Moskaitis, J. R., Baker, N. L., McCormack, J. P., Viner, K. C., McLay, J. G., Flatau, M. K., Xu, L., Chen, C.,
1063 and Chang, S. W.: The Navy Global Environmental Model. *Oceanography*, Special Issue on Navy Operational
1064 Models, 27, No. 3. 2014.

1065 Holben, B. N., Eck, T. F., Slutsker, I., Tanré, D., Buis, J. P., Setzer, A., Vermote, E., Reagan, J. A., Kaufman, Y. J.,
1066 Nakajima, T., Lavenu, F., Jankowiak, I., & Smirnov, A.: AERONET - A federated instrument network and data
1067 archive for aerosol characterization. *Remote Sensing of Environment*, 66(1), 1-16, [https://doi.org/10.1016/S0034-4257\(98\)00031-5](https://doi.org/10.1016/S0034-4257(98)00031-5), 1998.

1069 Huttunen, J., Arola, A., Myhre, G., Lindfors, A. V., Mielonen, T., Mikkonen, S., Schafer, J. S., Tripathi, S. N., Wild,
1070 M., Komppula, M., and Lehtinen, K. E. J.: Effect of water vapor on the determination of aerosol direct radiative
1071 effect based on the AERONET fluxes, *Atmos. Chem. Phys.*, 14, 6103–6110, [https://doi.org/10.5194/acp-14-6103-](https://doi.org/10.5194/acp-14-6103-2014)
1072 2014, 2014.

1073 Ibrahim, A., Franz, B.A., Ahmad, Z., and Bailey, S.W.: Multiband atmospheric correction algorithm for ocean color
1074 retrievals, *Front. Earth Sci.*, <https://doi.org/10.3389/feart.2019.00116>, 2019.

1075 Ichoku, C., Allen Chu, D., Mattoo, S., Kaufman, Y.J., Remer, L.A., Tanre, D., Slutsker, I., and Holben, B.N.: A
1076 spatio-temporal approach for global validation and analysis of MODIS aerosol products, *Geophysical Research*
1077 *Letters*, 29(12), <https://doi.org/10.1029/2001GL013206>, 2002.

1078 Jeong, J.I., and Park, R.J.: Winter monsoon variability and its impact on aerosol concentrations in East Asia,
1079 *Environmental Pollution*, Volume 221, Pages 285-292, <https://doi.org/10.1016/j.envpol.2016.11.075>, 2017.

1080 Jung, E., Albrecht, B., Prospero, J. M., Jonsson, H. H., & Kreidenweis, S. M.: Vertical structure of aerosols,
1081 temperature, and moisture associated with an intense African dust event observed over the eastern
1082 Caribbean. *Journal of Geophysical Research Atmospheres*, 118, 4623– 4643. <https://doi.org/10.1002/jgrd.50352>,
1083 2013.

1084 Kahn, R.A., Gaitley, B.J., Martonchik, J.V., Diner, D.J., Crean, K.A. and Holben, B.: Multiangle Imaging
1085 Spectroradiometer (MISR) global aerosol optical depth validation based on 2 years of coincident Aerosol Robotic
1086 Network (AERONET) observations. *Journal of Geophysical Research* 110: doi: 10.1029/2004JD004706. issn: 0148-
1087 0227, 2005.

1088 Kanitz, T., Ansmann, A., Seifert, P., Engelmann, R., Kalisch, J., & Althausen, D.: Radiative effect of aerosols above
1089 the northern and southern Atlantic Ocean as determined from shipborne lidar observations. *Journal of Geophysical*
1090 *Research; Atmospheres*, 118, 12,556– 12,565. <https://doi.org/10.1002/2013jd019750>, 2013.

1091 Kanitz, T., Engelmann, R., Heinold, B., Baars, H., Skupin, A., & Ansmann, A.: Tracking the Saharan air layer with
1092 shipborne lidar across the tropical atlantic. *Geophysical Research*
1093 *Letters*, 41, 1044– 1050. <https://doi.org/10.1002/2013gl058780>, 2014.

1094 Kannamadugu, H.B.S., Varghese, A.O., Mukkara, S.R., Joshi, A.K. and Moharil, S.V.: Discrimination of Aerosol
1095 Types and Validation of MODIS Aerosol and Water Vapour Products Using a Sun Photometer over Central
1096 India. *Aerosol Air Qual. Res.* 15: 682-693. <https://doi.org/10.4209/aaqr.2014.04.0088>, 2015.

1097 Karyampudi, V. M., Palm, S.P., Reagen, J.A., Fang, H., Grant, W.B, Hoff, R.M., Moulin, C., Pierce, H.F., Torres,
1098 O., Browell, E.V., and Melfi, S.H.: Validation of the Saharan dust plume conceptual model using Lidar, Meteosat,
1099 and ECMWF data, *Bull. Am. Meteorol. Soc.*, 80, 1045 – 1074, [https://doi.org/10.1175/1520-0477\(1999\)](https://doi.org/10.1175/1520-0477(1999)80<1045:VADP>2.0.CO;2), 1999.

1100 Kaufman, Y. J., and Fraser, R. S.: The effect of smoke particles on clouds and climate forcing, *Science*, 277, 1636-
1101 1639, DOI: 10.1126/science.277.5332.1636, 1997.

1102 Kim, S.-W., Chazette, P., Dulac, F., Sanak, J., Johnson, B., and Yoon, S.-C.: Vertical structure of aerosols and water
1103 vapor over West Africa during the African monsoon dry season, *Atmos. Chem. Phys.*, 9, 8017–8038,
1104 <https://doi.org/10.5194/acp-9-8017-2009>, 2009.

1105 Kleinman, L.I., and Daum, P.H.: Vertical distribution of aerosol particles, water vapor, and insoluble trace gases in
1106 convectively mixed air, *J. Geophys. Res. Atmos.*,96 (D1), 991-1005, <https://doi.org/10.1029/90JD02117>, 1991.

1107 Kuciauskas, A. P., Xian, P., Hyer, E. J., Oyola, M. I., & Campbell, J. R.: Supporting Weather Forecasters in
1108 Predicting and Monitoring Saharan Air Layer Dust Events as They Impact the Greater Caribbean, *Bulletin of the*
1109 *American Meteorological Society*, 99(2), 259-268, <https://doi.org/10.1175/BAMS-D-16-0212.1>, 2018.

1110 Kumar, K. R., Sivakumar, V., Reddy, R. R., Gopal, K. R., Adesina, A. J.: Inferring wavelength dependence of AOD
1111 and Ångström exponent over a sub-tropical station in South Africa using AERONET data: Influence of

1112 meteorology, long-range transport and curvature effect, *Science of The Total Environment*, 461, 397-408,
1113 <https://doi.org/10.1016/j.scitotenv.2013.04.095>, 2013.

1114 Kumar, K. R., Kang, N., Sivakumar, V., Griffith, D.: Temporal characteristics of columnar aerosol optical properties
1115 and radiative forcing (2011–2015) measured at AERONET's Pretoria_CSIR_DPSS site in South Africa,
1116 *Atmospheric Environment*, 165, 274-289, <https://doi.org/10.1016/j.atmosenv.2017.06.048>, 2017.

1117 Lee, E., Županski, M., Županski, D. and Park, S. K.: Impact of the OMI aerosol optical depth on analysis increments
1118 through coupled meteorology–aerosol data assimilation for an Asian dust storm, *Remote Sens. Environ.*, 193, 38–
1119 53, 30 doi:10.1016/j.rse.2017.02.013, 2017.

1120 Li, Q., Zhang, R., and Wang, Y.: Interannual variation of the wintertime fog-haze days across central and eastern
1121 China and its relation with East Asian winter monsoon, *International Journal of Climatology*, 36(1),
1122 <https://doi.org/10.1002/joc.4350>, 2016.

1123 Li, J., Liao, H., Hu, J., Li, N., Severe particulate pollution days in China during 2013-2018 and the associated typical
1124 weather patterns in Beijing-Tianjin-Hebei and the Yangtze River Delta regions. *Environmental Pollution*, 248, 74-
1125 81, <https://doi.org/10.1016/j.envpol.2019.01.124>, 2019.

1126 Liu, Z., Liu, Q., Lin, H. C., Schwartz, C. S., Lee, Y. H. and Wang, T.: Three-dimensional variational assimilation of
1127 MODIS aerosol optical depth: Implementation and application to a dust storm over East Asia, *J. Geophys. Res.*
1128 *Atmos.*, 116(23), 1– 19, doi:10.1029/2011JD016159, 2011.

1129 Liu, D., Zhao, T., Boiyo, R., Chen, S., Lu, Z., Wu, Y., Zhao, Y.: Vertical structures of dust aerosols over East Asia
1130 based on CALIPSO retrievals. *Remote Sens.*, 11,701; doi:10.3390/rs11060701, 2019.

1131 Livingston, J. M., Russell, P. B., Reid, J. S., Redemann, J., Schmidt, B., Allen, D. A., Torres, O., Levy, R. C.,
1132 Remer, L. A., Holben, B. N., Smirnov, A., Dubovik, O., Welton, E. J., Campbell, J. R., Wang, J., Christopher, S.
1133 A.: Airborne Sun photometer measurements of aerosol optical depth and columnar water vapor during the Puerto
1134 Rico Dust Experiment and comparison with land, aircraft, and satellite measurements, *J. Geophys. Res.*, 108, 8588,
1135 doi:10.1029/2002JD002520, D19, 2003.

1136 Luo, B., Minnett, P.J., Gentemann, C., and Szczodrak, G.: Improving satellite retrieved night-time infrared sea
1137 surface temperatures in aerosol contaminated regions. *Remote Sensing of Environment*, 223,8-20,
1138 <https://doi.org/10.1016/j.rse.2019.01.009>, 2019.

1139 Lynch, P., Reid, J. S., Westphal, D. L., Zhang, J., Hogan, T. F., Hyer, E. J., Curtis, C. A., Hegg, D. A., Shi, Y.,
1140 Campbell, J. R., Rubin, J. I., Sessions, W. R., Turk, F. J., and Walker, A. L.: An 11-year global gridded aerosol
1141 optical thickness reanalysis (v1.0) for atmospheric and climate sciences, *Geosci. Model Dev.*, 9, 1489–1522,
1142 <https://doi.org/10.5194/gmd-9-1489-2016>, 2016.

1143 Marsham, J. H., Parker, D. J., Grams, C. M., Johnson, B. T., Grey, W. M. F., & Ross, A. N.: Observations of
1144 mesoscale and boundary-layer scale circulations affecting dust transport and uplift over the Sahara. *Atmospheric*
1145 *Chemistry and Physics*, 8(23), 6979– 6993, <https://doi.org/10.5194/acp-8-6979-2008>, 2008.

1146 Marsham, J. H., Parker, D. J., Todd, M. C., Banks, J. R., Brindley, H. E., Garcia-Carreras, L., Roberts, A. J., and
1147 Ryder, C. L.: The contrasting roles of water and dust in controlling daily variations in radiative heating of the
1148 summertime Saharan heat low, *Atmos. Chem. Phys.*, 16, 3563–3575, <https://doi.org/10.5194/acp-16-3563-2016>,
1149 2016.

1150 Martins, V. S., Novo, E. M. L. M., Lyapustin, A., Aragão, L. E. O. C., Freitas, S. R., Barbosa, C. C. F: Seasonal and
1151 interannual assessment of cloud cover and atmospheric constituents across the Amazon (2000–2015): Insights for
1152 remote sensing and climate analysis, *ISPRS Journal of Photogrammetry and Remote Sensing*, 145, 309-327,
1153 <https://doi.org/10.1016/j.isprsjprs.2018.05.013>, 2018.

1154 Ménard, R., Gauthier, P., Rochon, Y., Robichaud, A., de Grandpré, J., Yang, Y., Charette, C., and Chabrilat, S.:
1155 Coupled Stratospheric Chemistry–Meteorology Data Assimilation. Part II: Weak and Strong
1156 Coupling. *Atmosphere*, 10, 798, <https://doi.org/10.3390/atmos10120798> , 2019.

1157 Mortier, A., Goloub, P., Derimian, Y., Tanre, D., Podvin, T., Blarel, L., Deroo, C., Marticorena, B., Diallo, A., and
1158 Ndiaye, T.: Climatology of aerosol properties and clear-sky shortwave radiative effects using Lidar and Sun
1159 photometer observations in the Dakar site, *J. Geophys. Res. Atmos.*, 121(11),
1160 <https://doi.org/10.1002/2015JD024588>, 2016.

1161

1162 O'Neill, N. T., Royer, A., Coté, P., McArthur, L. J. B., Relations between optically derived aerosol parameters,
 1163 humidity, and air-quality data in an urban atmosphere, *J. Appl Meteor.*, 32, 1484-1498,
 1164 [https://doi.org/10.1175/1520-0450\(1993\)032<1484:RBODAP>2.0.CO;2](https://doi.org/10.1175/1520-0450(1993)032<1484:RBODAP>2.0.CO;2), 1993.

1165 Patadia, F., Levy, R. C., and Mattoo, S.: Correcting for trace gas absorption when retrieving aerosol optical depth
 1166 from satellite observations of reflected shortwave radiation, *Atmos. Meas. Tech.*, 11, 3205–3219,
 1167 <https://doi.org/10.5194/amt-11-3205-2018>, 2018.

1168 Perez-Ramirez, D., Whiteman, D.N., Smirnov, A., Lyamani, H., Holben, B.N., Pinker, R., Andrade, M., Alados-
 1169 Arboledas, L.: Evaluation of AERONET precipitable water vapor versus microwave radiometry, GPS, and
 1170 radiosondes at ARM sites, *J. Geophys. Res. Atmos.*, 119(15), <https://doi.org/10.1002/2014JD021730>, 2014.

1171 Perry, K.D., and Hobbs P.V.: Influences of isolated cumulus clouds on the humidity of their surroundings *Journal of*
 1172 *the Atmospheric Sciences*. 53: 159-174. DOI: [https://doi.org/10.1175/1520-](https://doi.org/10.1175/1520-0469(1996)053<0159:IOICCO>2.0.CO;2)
 1173 [0469\(1996\)053<0159:IOICCO>2.0.CO;2](https://doi.org/10.1175/1520-0469(1996)053<0159:IOICCO>2.0.CO;2), 1996.

1174 Pistone, K., Praveen, P. S., Thomas, R. M., Ramanathan, V., Wilcox, E. M., and Bender, F. A.-M.: Observed
 1175 correlations between aerosol and cloud properties in an Indian Ocean trade cumulus regime, *Atmos. Chem. Phys.*,
 1176 16, 5203–5227, <https://doi.org/10.5194/acp-16-5203-2016>, 2016.

1177 Pistone, K., Zuidema, P., Wood, R., Diamond, M., da Silva, A. M., Ferrada, G., Saide, P. E., Ueyama, R., Ryoo, J.-
 1178 M., Pfister, L., Podolske, J., Noone, D., Bennett, R., Stith, E., Carmichael, G., Redemann, J., Flynn, C., LeBlanc, S.,
 1179 Segal-Rozenhaimer, M., and Shinozuka, Y.: Exploring the elevated water vapor signal associated with the free
 1180 tropospheric biomass burning plume over the southeast Atlantic Ocean, *Atmos. Chem. Phys.*, 21, 9643–9668,
 1181 <https://doi.org/10.5194/acp-21-9643-2021>, 2021.

1182 Radke L.F., and Hobbs, P.V.: Humidity and particle fields around some small cumulus clouds, *Journal of the*
 1183 *Atmospheric Sciences*. 48: 1190-1193. DOI: 10.1175/1520-0469(1991), 1991.

1184 Reid, J. S., Kinney, J. E., Westphal, D. L., Holben, B. N., Welton, E. J., Tsay, S.-C., Christopher, S. A., Eleuterio,
 1185 D. P., Campbell, J. R., Jonsson, H. H., Livingston, J. M., Maring, H. B., Meier, M., Pilewskie, P., Reid, E. A.,
 1186 Russell, P. B., Savoie, D., Smirnov, A., and D. Tanré D.: Analysis of measurements of Saharan dust by airborne
 1187 and ground-based remote sensing methods during the Puerto Rico Dust Experiment (PRIDE), *J. Geophys. Res.*, 108,
 1188 8586, doi:10.1029/2002JD002493, D19, 2003.

1189 Reid, J. S., Piketh, S., Burger, R., Ross, K., Jensen, T., Bruintjes, R., Walker, A., Al Mandoos, A., Miller, S., Hsu,
 1190 C., Kuciauskas, A., and Westphal, D. L.: An overview of UAE2 flight operations: Observations of summertime
 1191 atmospheric thermodynamic and aerosol profiles of the southern Arabian Gulf, *J. Geophys. Res.*, 113, D14213,
 1192 doi:10.1029/2007JD009435, 2008.

1193 Reid, J. S., Hyer, E. J., Johnson, R., Holben, B. N., Yokelson, R. J., Zhang, J., Campbell, J.R., Christopher, S.A., Di
 1194 Girolamo, L., Giglio, L., Holz, R.E., Kearney, C., Miettinen, J., Reid, E.A., Turk, F.J., Wang, J., Xian, P., Zhao, G.,
 1195 Balasubramanian, R., Chew, B.N., Janjai, S., Lagrosas, N., Lestari, P., Lin, N.-H., Mahmud, M., Nguyen, A.X.,
 1196 Norris, B., Oanh, N.T.K., Oo, M., Salinas, S.V., Welton, E.J., and Liew, S.C.: Observing and understanding the
 1197 Southeast Asian aerosol system by remote sensing: An initial review and analysis for the Seven Southeast Asian
 1198 Studies (7SEAS) program. *Atmospheric Research*, 122, 403–468. <https://doi.org/10.1016/j.atmosres.2012.06.005>,
 1199 2013.

1200 Reid, J. S., Posselt, D. J., Kaku, K., Holz, R. A., Chen, G., Eloranta, E. W., Kuehn, R. E., Woods, S., Zhang, J.,
 1201 Anderson, B., Bui, T. P., Diskin, G. S., Minnis, P., Newchurch, M. J., Tanelli, S., Trepte, C. R., Thornhill, K. L., and
 1202 Ziemba, L. D.: Observations and hypotheses related to low to middle free tropospheric aerosol, water vapor and
 1203 altocumulus cloud layers within convective weather regimes: a SEAC4RS case study, *Atmos. Chem. Phys.*, 19,
 1204 11413–11442, <https://doi.org/10.5194/acp-19-11413-2019>, 2019.

1205 Reid, J.S., Gumber, A., Zhang, J., Holz, R.E., Rubin, J.I., Xian, P., Smirnov, A., Eck, T.F., O'Neill, N.T., Levy
 1206 R.C., Reid, E.A., Colarco, P.R., Benedetti, A., Tanaka, T.: A Coupled Evaluation of Operational MODIS and Model
 1207 Aerosol Products for Maritime Environments Using Sun Photometry: Evaluation of the Fine and Coarse
 1208 Mode. *Remote Sensing*; 14(13):2978. <https://doi.org/10.3390/rs14132978>, 2022.

1209 Remer, L.A., Tanre, D., Kaufman, Y.J., Ichoku, C., Mattoo, S., Levy, R., Chu, D.A., Holben, B., Dubovik, O.,
 1210 Smirnov, A., Martins, J.V., Li, R.-R., and Ahmad, Z.: Validation of MODIS aerosol retrieval over ocean,
 1211 Geophysical Research Letters, 29(12), 1618, <https://doi.org/10.1029/2001GL013204>, 2002.

1212 Resquin, M.D., Santagata, D., Gallardo, L., Gomez, D., Rossler, C., Dawidowski, L.: Local and remote black carbon
 1213 sources in the Metropolitan Area of Buenos Aires. Atmospheric Environment. Volume 182, Pages 105-114,
 1214 <https://doi.org/10.1016/j.atmosenv.2018.03.018>, 2018.

1215 Rosário, N. E., Yamasoe, M. A., Brindley, H., Eck, T. F., and Schafer, J.: Downwelling solar irradiance in the
 1216 biomass burning region of the southern Amazon: Dependence on aerosol intensive optical properties and role of
 1217 water vapor, J. Geophys. Res., 116, D18304, doi:10.1029/2011JD015956, 2011.

1218 [Rubin, J. I., Reid, J. S., Hansen, J. A., Anderson, J. L., Collins, N., Hoar, T. J., Hogan, T., Lynch, P., McLay, J.,
 1219 Reynolds, C. A., Sessions, W. R., Westphal, D. L., and Zhang, J.: Development of the Ensemble Navy Aerosol
 1220 Analysis Prediction System \(ENAAAPS\) and its application of the Data Assimilation Research Testbed \(DART\) in
 1221 support of aerosol forecasting. Atmos. Chem. Phys., 16, 3927–3951, <https://doi.org/10.5194/acp-16-3927-2016>,
 1222 2016.](#)

1223 Ryder, C. L.: Radiative effects of increased water vapor in the upper Saharan Air Layer associated with enhanced
 1224 dustiness. Journal of Geophysical Research: Atmospheres, 126, e2021JD034696,
 1225 <https://doi.org/10.1029/2021JD034696>, 2021.

1226 Sano, I., Mukai, S., Yamao, M., Takamura, T., Nakajima, T., and Holben, B.: Calibration and Validation of
 1227 Retrieved Aerosol Properties Based on AERONET and SKYNET, Advances in Space Research 32 (11): 2159–
 1228 2164. doi:10.1016/S0273-1177(03)00685-9, 2003.

1229 Schneider, T., O’Gorman, P.A., and Levine, X.J.: Water vapor and the dynamics of climate changes, Rev. Geophys.,
 1230 48, RG3001, doi:10.1029/2009RG000302, 2010.

1231 Sessions, W. R., Reid, J. S., Benedetti, A., Colarco, P. R., da Silva, A., Lu, S., Sekiyama, T., Tanaka, T. Y.,
 1232 Baldasano, J. M., Basart, S., Brooks, M. E., Eck, T. F., Iredell, M., Hansen, J. A., Jorba, O. C., Juang, H.-M. H.,
 1233 Lynch, P., Morcrette, J.-J., Moorthi, S., Mulcahy, J., Pradhan, Y., Razinger, M., Sampson, C. B., Wang,
 1234 J., and Westphal, D. L.: Development towards a global operational aerosol consensus: basic climatological
 1235 characteristics of the International Cooperative for Aerosol Prediction Multi-Model Ensemble (ICAP-MME),
 1236 Atmos. Chem. Phys., 15, 335–362, doi:10.5194/acp-15-335-2015, 2015.

1237 Sherwood, S.C., Roca, R., Weckwerth, T.M., and Andronova, N.G.: Tropospheric water vapor, convection, and
 1238 climate, Rev. Geophys., 48, RG2001, doi:10.1029/2009RG000301, 2010.

1239 Shi, Y. R., Levy, R. C., Eck, T. F., Fisher, B., Mattoo, S., Remer, L. A., Slutsker, I., and Zhang, J.: Characterizing
 1240 the 2015 Indonesia fire event using modified MODIS aerosol retrievals, Atmos. Chem. Phys., 19, 259–274,
 1241 <https://doi.org/10.5194/acp-19-259-2019>, 2019.

1242 Smirnov, A., Royer, A., O’Neill, N. T., and Tarussov, A.: A study of the link between synoptic air mass type and
 1243 atmospheric optical parameters, J. Geophys. Res., 99(D10), 20967– 20982, doi:10.1029/94JD01719, 1994.

1244 Sobrino, J.A., Li, Z.-L., and Stoll, M. P.: Impact of the atmospheric transmittance and total water vapor content in
 1245 the algorithms for estimating satellite sea surface temperatures, *IEEE Transactions on Geoscience and Remote
 1246 Sensing*, vol. 31, no. 5, pp. 946-952, doi: 10.1109/36.263765, 1993.

1247 Späth, F., Behrendt, A., Muppa, S. K., Metzendorf, S., Riede, A., and Wulfmeyer, V.: 3-D water vapor field in the
 1248 atmospheric boundary layer observed with scanning differential absorption lidar, Atmos. Meas. Tech., 9, 1701–
 1249 1720, <https://doi.org/10.5194/amt-9-1701-2016>, 2016.

1250 Spyrou C.: Direct radiative impacts of desert dust on atmospheric water content, Aerosol Science and
 1251 Technology, 52:6, 693-701, DOI: 10.1080/02786826.2018.1449940, 2018.

1252 Stull, R. B. and Eloranta, E. W.: Boundary Layer Experiment 1983, Bull. Amer. Meteorol. Soc., 65, 450–456, DOI:
 1253 10.1175/1520-0477(1984)065<0450:BLE>2.0.CO;2, 1984.

Formatted: Font: (Default) Times New Roman, 10 pt,
 Font color: Auto, English (United Kingdom), Pattern:
 Clear

1254 Su, H., Jiang, J.H., Liu, X., Penner, J.E., Read, W.G., Massie, S., Schoeberl, M.R., Colarco, P., Livesey, N.J., and
1255 Santee, M.L.: Observed increase of TTL temperature and water vapor in polluted clouds over Asia, *Journal of*
1256 *Climate*, 24(11), 2728-2736, <https://doi.org/10.1175/2010JCLI3749.1>, 2011.

1257 Ten Hoeve, J. E., Remer, L. A., and Jacobson, M. Z.: Microphysical and radiative effects of aerosols on warm
1258 clouds during the Amazon biomass burning season as observed by MODIS: impacts of water vapor and land cover,
1259 *Atmos. Chem. Phys.*, 11, 3021–3036, <https://doi.org/10.5194/acp-11-3021-2011>, 2011.

1260 Tesche, M., Gross, S., Ansmann, A., Müller, D., Althausen, D., Freudenthaler, V., and Esselborn, M.: Profiling of
1261 Saharan dust and biomass-burning smoke with multiwavelength polarization Raman lidar at Cape Verde, *Tellus B*,
1262 63B, 649-676, DOI: 10.1111/j.1600-0889.2011.00548.x, 2011.

1263 Turner D.D., Ferrare, R.A., Heilman Brasseur, L.A., Feltz, W.F., and Tooman, T.P.: Automated Retrievals of Water
1264 Vapor and Aerosol Profiles from an Operational Raman Lidar. *J.*
1265 *Atmos. Oceanic Tech*, 19, 37-50, DOI:10.1175/1520-0426(2002), 2002.

1266 Veselovskii, I., Goloub, P., Podvin, T., Bovchaliuk, V., Derimian, Y., Augustin, P., Fourmentin, M., Tanre, D.,
1267 Korenskiy, M., Whiteman, D. N., Diallo, A., Ndiaye, T., Kolgotin, A., and Dubovik, O.: Retrieval of optical and
1268 physical properties of African dust from multiwavelength Raman lidar measurements during the SHADOW
1269 campaign in Senegal, *Atmos. Chem. Phys.*, 16, 7013–7028, doi:10.5194/acp-16-7013-2016, 2016.

1270 Wang, Y., Hua, D., Wang, L., Tang, J., Mao, J., and Kobayashi, T.: Observations and analysis of relationship
1271 between water vapor and aerosols using raman lidar, *Jpn. J. Appl. Phys.*, 51, 102401,
1272 <http://dx.doi.org/10.1143/JJAP.51.102401>, 2012.

1273 Wang, J., Gei, C., Yang, Z., Hyer, E. J., Reid, J. S., Chew, B. N., Mahmud M.: Mesoscale modeling of smoke
1274 transport over the Southeast Asian Maritime Continent: interplay of sea breeze, trade wind, typhoon, and
1275 topography, *Atmos. Res.*, 122, 486-503, <https://doi.org/10.1016/j.atmosres.2012.05.009>, 2013.

1276 Wang, H., Xu, J., Zhang, M., Yang, Y., Shen, X., Wang, Y., Chen, D., Guo, J. A Study of the meteorological causes
1277 of a prolonged and severe haze episode in January 2013 over central-eastern China, *Atmospheric Environment*, 98,
1278 146-157, <https://doi.org/10.1016/j.atmosenv.2014.08.053>, 2014.

1279 Wang, L. T., Wei, Z., Yang, J., Zhang, Y., Zhang, F. F., Su, J., Meng, C. C., and Zhang, Q.: The 2013 severe haze
1280 over southern Hebei, China: model evaluation, source apportionment, and policy implications, *Atmos. Chem. Phys.*,
1281 14, 3151–3173, <https://doi.org/10.5194/acp-14-3151-2014>, 2014.

1282 Wimmers, A. J., C. S. Velden: Seamless Advective Blending of Total Precipitable Water Retrievals from Polar-
1283 Orbiting Satellites. *J. Appl. Meteor. Climatol.*, 50, 1024-1036. doi: <http://dx.doi.org/10.1175/2010JAMC2589.1>,
1284 2011.

1285 Wong, S., Dessler, A. E., Mahowald, N. M., Yang, P., & Feng, Q.: Maintenance of lower tropospheric temperature
1286 inversion in the Saharan air layer by dust and dry anomaly. *Journal of*
1287 *Climate*, 22(19), 5149– 5162. <https://doi.org/10.1175/2009jcli2847.1>, 2009.

1288 Yu, S., Alapaty, K., Mathur, R., Pleim, J., Zhang, Y., Nolte, C., Eder, B., Foley, K., and Nagashima, Attribution of
1289 the United States “warming hole”: Aerosol indirect effect and precipitable water vapor, *Sci Rep*, 4, 6929,
1290 <https://doi.org/10.1038/srep06929>, 2014.

1291 Yu, L., Zhang, M., Wang, L., Lu, Y., and Li, J.: Effects of aerosols and water vapour on spatial-temporal variations
1292 of the clear-sky surface solar radiation in China, *Atmospheric Research*, 248, 105162,
1293 <https://doi.org/10.1016/j.atmosres.2020.105162>, 2021.

1294 Yufeng, W., Qiang, F., Meina, Z., Fei, G., Huige, D., Yuehui, S., Dengxin, A.: UV multifunctional Raman lidar
1295 system for the observation and analysis of atmospheric temperature, humidity, aerosols and their conveying
1296 characteristics over Xi’an, *J. of Quant Spect. And Rad. Trans*, 205, 114-126,
1297 <https://doi.org/10.1016/j.jqsrt.2017.10.001>, 2018.

1298 Xian, P., Reid, J., Hyer, E., Sampson, C. Rubin, J., Ades, M., Asencio, N., Basart, S., Benedetti, A., Bhattacharjee,
1299 P.S., Brooks, M.E., Colarco, P.R., da Silva, A.M., Eck, T.F., Guth, J., Jorba, O., Kouznetsov, R., Kipling, Z., Sofiev,
1300 M., Perez Garcia-Pando, C., Pradhan, Y., Tanaka, T., Wang, J., Westphal, D.L., Yumimoto, K., and Zhang, J.:
1301 Current state of the global operational aerosol multi-model ensemble: An update from the International Cooperative
1302 for Aerosol Prediction (ICAP). *Q.J.R. Meteorol. Soc.* 145 (Suppl. 1): 176-209, DOI: 10.1002/qj.3497, 2019.

1303 Xian, P., Klotzbach, P. J., Dunion, J. P., Janiga, M. A., Reid, J. S., Colarco, P. R., and Kipling, Z.: Revisiting the
1304 relationship between Atlantic dust and tropical cyclone activity using aerosol optical depth reanalyses: 2003–2018,
1305 *Atmos. Chem. Phys.*, 20, 15357–15378, <https://doi.org/10.5194/acp-20-15357-2020>, 2020.

1306 Zeng, Z.-C., Zhang, Q., Natraj, V., Margolis, J. S., Shia, R.-L., Newman, S., Fu, D., Pongetti, T. J., Wong, K. W.,
1307 Sander, S. P., Wennberg, P. O., and Yung, Y. L.: Aerosol scattering effects on water vapor retrievals over the Los
1308 Angeles Basin, *Atmos. Chem. Phys.*, 17, 2495–2508, <https://doi.org/10.5194/acp-17-2495-2017>, 2017.

1309 Zhang, J., Reid, J.S., Westphal, D.L., Baker, N.L., and Hyer, E.J.: A system for operational aerosol optical depth
1310 data assimilation over global oceans, *Journal of Geophysical Research: Atmospheres*, 113(D10),
1311 <https://doi.org/10.1029/2007JD009065>, 2008.

1312 Zhang, J., Wang, S., Guo, Y., Zhang, R., Qin, X., Huang, K., Wang, D., Fu, Q., Wang, J., and Zhou, B.: Aerosol
1313 vertical profile retrieved from ground-based MAX-DOAS observation and characteristic distribution during the
1314 wintertime in Shanghai, China, *Atmospheric Environment*, 192, 193-205,
1315 <https://doi.org/10.1016/j.atmosenv.2018.08.051>, 2018.

1316 Zhu, J., Che, H., Xia, X., Yu, X., Wang, J.: Analysis of water vapor effects on aerosol properties and direct radiative
1317 forcing in China, *Science of The Total Environment*, 650, 257-266, <https://doi.org/10.1016/j.scitotenv.2018.09.022>,
1318 2019.